



HAL
open science

Imaging diffuse clouds: bright and dark gas mapped in CO

H. S. Liszt, J. Pety

► **To cite this version:**

H. S. Liszt, J. Pety. Imaging diffuse clouds: bright and dark gas mapped in CO. Astronomy and Astrophysics - A&A, 2012, 541, pp.58. 10.1051/0004-6361/201218771 . hal-00674993

HAL Id: hal-00674993

<https://hal.science/hal-00674993>

Submitted on 28 Feb 2012

HAL is a multi-disciplinary open access archive for the deposit and dissemination of scientific research documents, whether they are published or not. The documents may come from teaching and research institutions in France or abroad, or from public or private research centers.

L'archive ouverte pluridisciplinaire **HAL**, est destinée au dépôt et à la diffusion de documents scientifiques de niveau recherche, publiés ou non, émanant des établissements d'enseignement et de recherche français ou étrangers, des laboratoires publics ou privés.

Imaging diffuse clouds: Bright and dark gas mapped in CO [★]

H. S. Liszt¹, J. Pety^{2,3}

¹ National Radio Astronomy Observatory, 520 Edgemont Road, Charlottesville, VA, USA 22903-2475

² Institut de Radioastronomie Millimétrique, 300 Rue de la Piscine, F-38406 Saint Martin d'Hères, France

³ Obs. de Paris, 61 av. de l'Observatoire, 75014, Paris, France

received February 28, 2012

ABSTRACT

Aims. We wish to relate the degree scale structure of galactic diffuse clouds to sub-arcsecond atomic and molecular absorption spectra obtained against extragalactic continuum background sources.

Methods. We used the ARO 12m telescope to map J=1-0 CO emission at 1' resolution over 30' fields around the positions of 11 background sources occulted by 20 molecular absorption line components, of which 11 had CO emission counterparts. We compare maps of CO emission to sub-arcsec atomic and molecular absorption spectra and to the large-scale distribution of interstellar reddening.

Results. 1) The same clouds, identified by their velocity, were seen in absorption and emission and atomic and molecular phases, not necessarily in the same direction. Sub-arcsecond absorption spectra are a preview of what is seen in CO emission away from the continuum. 2) The CO emission structure was amorphous in 9 cases, quasi-periodic or wave-like around B0528+134 and tangled and filamentary around BL Lac. 3) Strong emission, typically 4-5 K at $E_{B-V} \leq 0.15$ mag and up to 10-12 K at $E_{B-V} \lesssim 0.3$ mag was found, much brighter than toward the background targets. Typical covering factors of individual features at the 1 K km s⁻¹ level were 20%. 4) CO-H₂ conversion factors as much as 4-5 times below the mean value $N(\text{H}_2)/W_{\text{CO}} = 2 \times 10^{20} \text{ H}_2 \text{ cm}^{-2} (\text{K km s}^{-1})^{-1}$ are required to explain the luminosity of CO emission at/above the level of 1 K km s⁻¹. Small conversion factors and sharp variability of the conversion factor on arcminute scales are due primarily to CO chemistry and need not represent unresolved variations in reddening or total column density.

Conclusions. Like FERMI and PLANCK we see some gas that is dark in CO and other gas in which CO is overluminous per H₂. A standard CO-H₂ conversion factor applies overall owing to balance between the luminosities per H₂ and surface covering factors of bright and dark CO, but with wide variations between sightlines and across the faces of individual clouds.

Key words. interstellar medium – molecules

1. Introduction

With somewhat imprecise boundaries, interstellar clouds are generally classed as diffuse, $A_V \lesssim 1$ mag, or dark, $A_V \gtrsim 4-6$ mag, with an intermediate translucent regime (Snow & McCall, 2006). In diffuse clouds the dominant form of carbon is C⁺ and hydrogen is mostly atomic, although with a very significant overall admixture of H₂, 25% or more as a global average (Savage et al., 1977; Liszt et al., 2010). In dark or molecular clouds the carbon is overwhelmingly in CO with an admixture of C I and the hydrogen resides almost entirely in H₂. The population of diffuse clouds is sometimes called H I clouds in radio astronomical terms.

The shadows of dark clouds are seen outlined against brighter background fields and the clouds themselves are often imaged in the mm-wave emission of CO and many other species: the ¹²CO(1-0) sky (Dame et al., 2001) is usually (and in part incorrectly, see below) understood as a map of fully-molecular clouds. The shadows of H I or diffuse clouds are their absorption-line spectra and for the most part, individual diffuse clouds are known only as kinematic features in optical and/or radio absorption spectra. No means exist to image individual diffuse clouds at optical wavelengths and attempts to map in-

dividual H I clouds at radio wavelengths are generally frustrated by the blending and overlapping of contributions from multiple clouds and gas phases. This lack of identity has greatly complicated our ability to define diffuse clouds physically because absorption lines do not generally permit a direct determination of the cloud size or internal density.

When diffuse clouds discovered in absorption-line spectra have a sufficiently high complement of molecules they may be imaged at radio wavelengths in species such as OH and CH and, most usefully, CO. Despite a low fractional abundance of CO relative to H₂, $\langle X(\text{CO}) \rangle = 3 \times 10^{-6}$ (Burgh et al., 2007), mapping is facilitated by an enhanced brightness of the J=1-0 line in diffuse gas: the temperature is somewhat elevated ($T_K \gtrsim 25$ K), the density is comparatively small at typical ambient thermal pressure (Jenkins & Tripp, 2011) and the rotation ladder is subthermally excited. In accord with theory (Goldreich & Kwan, 1974), it is found observationally that there is a simple, linear proportionality between the integrated intensity W_{CO} of the CO J=1-0 lines and the CO column density, even when the gas is optically thick: $N(\text{CO}) \approx 10^{15} \text{ cm}^{-2} W_{\text{CO}} / \text{K km s}^{-1}$ for $W_{\text{CO}} \approx 0.2 - 6 \text{ K km s}^{-1}$ (Liszt & Lucas, 1998; Liszt, 2007). Per molecule, the ratio $W_{\text{CO}}/N(\text{CO})$ is 30-50 times higher in diffuse gas, compared to conditions in dense shielded fully-molecular gas where the rotation ladder is thermalized (Liszt et al., 2010). Of course this is of substantial assistance in the present work. Conversely, the high brightness (5-12 K) of many of lines we detected should not be taken as discrediting their origin in diffuse gas.

Send offprint requests to: H. S. Liszt

* Based on observations obtained with the ARO Kitt Peak 12m telescope.

Correspondence to: hliszt@nrao.edu

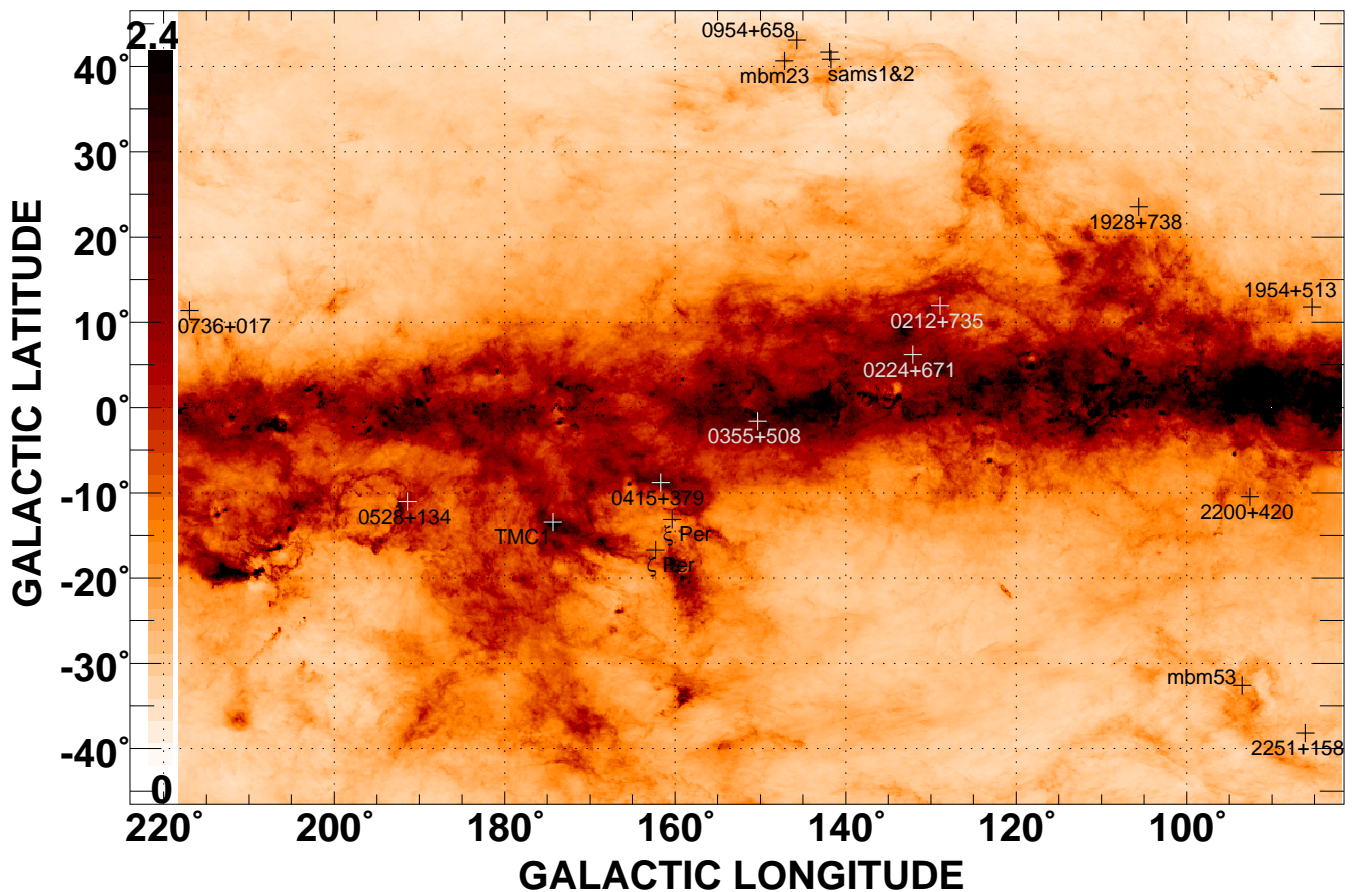


Fig. 1. Outer-galaxy finding chart for the sources studied here except B1730-130 at $l = 12^\circ$, see Table 1. The colored background is reddening at $6'$ resolution (Schlegel et al., 1998) truncated at a maximum of 2.4 mag as shown on the bar scale at left. Positions of continuum sources are indicated (see Table 1) along with a few other objects: the high-latitude molecular clouds MBM23 and MBM 53 (Magnani et al., 1985); TMC-1; SAMS 1 and 2 (Heithausen, 2004); and two Perseus stars commonly used for optical absorption line studies.

Earlier we showed that, in the mean, CO-H₂ conversion factors are similar in diffuse and dense fully molecular gas (Liszt et al., 2010), because the small abundance of CO relative to H₂ in diffuse gas is compensated by a much higher brightness per CO molecule. But the proportionality between W_{CO} and $N(\text{CO})$ in diffuse gas, where CO represents such a small fraction of the available gas phase carbon, means that the CO map of a diffuse cloud is really an image of the CO chemistry. Moreover the CO abundance exhibits extreme sensitivities to local conditions that are manifested as order of magnitude scatter in $N(\text{CO})/N(\text{H}_2)$ in optical absorption line studies (Sonnentrucker et al., 2007; Burgh et al., 2007; Sheffer et al., 2007, 2008), even beyond the often-rapid variation of $N(\text{H}_2)$ with $E_{\text{B-V}}$ (Savage et al., 1977) ($E_{\text{B-V}} \approx A_{\text{V}}/3.1$). The net result is that the CO emission map of a diffuse cloud can only indirectly be interpreted as tracing the underlying mass distribution, or even that of the H₂. Nonetheless, it should (we hope) provide some impression of the nature of the host gas, especially in the absence of any other means of ascertaining this.

In this paper we present maps of CO J=1-0 emission at arcminute resolution over 11 sky fields, typically $30' \times 30'$ around the positions of compact extragalactic mm-wave continuum sources that we have long used as targets for absorption line studies of the chemistry of diffuse clouds. As is the case for nearly all background sources seen at galactic latitudes $|b| < 15 - 18^\circ$, and for some sources at higher latitudes, the current targets were known to show absorption from HCO⁺ and

from one or more other commonly-detected species (OH, CO, C₂H, C₃H₂); most but not all directions also were known to show CO emission in at least some of the kinematic features present in absorption.

This work is organized as follows. The observational material discussed here is summarized in Sect. 2. In Sects. 3-5 we discuss the new maps with sources grouped in order of kinematic complexity. Sect. 6 is an intermediate summary of the lessons drawn from close scrutiny of the maps. Sect. 7 briefly discusses the influences of galactic and internal cloud kinematics and Sect. 8 presents a comparison of CO intensity and reddening within a few of the simpler individual fields. Online Appendix A shows a few position-velocity diagrams that, while of interest, could be considered redundant with those shown in the main text in Figs. 13 and 14. Figures B.1 and B.2 in online Appendix B show the target lines of sight in the context of large-scale galactic kinematics sampled in H I emission.

2. Observational material

2.1. CO J=1-0 emission

On-the-fly maps of CO J=1-0 emission were made at the ARO 12m telescope in 2008 December, 2009 January and 2009 December in generally poor weather using filter banks with 100 kHz or 0.260 km s^{-1} channel spacing and spectral resolution. System temperatures were typically 450 – 750 K. The data were subsequently put onto $20''$ pixel grids using the AIPS tasks

Table 1. Continuum target, line of sight and map field properties¹

| Target | ra (J2000) | dec (J2000) | l | b | Map size | E_{B-V} ² mag | $N(H I)$ ³ 10^{20} cm^{-2} | $N(H_2)$ ⁴ 10^{20} cm^{-2} | f_{H_2} ⁷ | W_{CO} K km s^{-1} | $\langle W_{CO} \rangle$ K km s^{-1} |
|-----------|---------------|----------------|--------|--------|-------------|-------------------------------|--|--|------------------------|----------------------------------|--|
| B0736+017 | 07:39:18.03 | 01:37:04.6 | 216.99 | 11.38 | 15' | 0.13 | 7.7 | 3.3 | 0.46 | 0.8 | 0.4 |
| B0954+658 | 09:58:47.24 | 65:33:54.7 | 145.75 | 43.13 | 30' | 0.12 | 5.3 ⁵ | 4.8 | 0.64 | 1.6 | 0.6 |
| B1730-130 | 17:33:02.66 | -13:04:49.5 | 12.03 | 10.81 | 30' | 0.53 | 28.3 | 4.3 | 0.23 | 0.4 | 0.4 |
| B1928+738 | 19:27:48.58 | 73:58:01.6 | 105.63 | 23.54 | 20' | 0.13 | 7.2 ⁵ | 2.7 | 0.43 | <0.2 | 0.0 |
| B1954+513 | 19:55:42.69 | 51:31:48.5 | 85.30 | 11.76 | 30' | 0.15 | 12.7 ⁵ | 5.0 | 0.44 | 1.6 | 0.3 |
| B2251+158 | 22:53:57.71 | 16:08:53.4 | 86.11 | -38.18 | 30' | 0.10 | 4.6 | 1.2 | 0.34 | 0.8 | 0.2 |
| B0528+134 | 05:30:46.41 | 13:31:55.1 | 191.37 | -11.01 | 30' | 0.89 | 30.9 | 7.9 | 0.34 | 2.2 | 2.6 |
| B2200+420 | 22:02:43.24 | 42:16:39.9 | 92.59 | -10.44 | 30' | 0.33 | 9.7 | 8.8 | 0.66 | 5.8 | 3.7 |
| B0212+735 | 02:17:30.81 | 73:49:32.6 | 128.93 | 11.96 | 30' | 0.76 | 32.1 | 18.6 | 0.54 | 5.8 | 1.56 |
| B0224+671 | 02:28:50.03 | 67:21:31.3 | 132.12 | 6.23 | 30' | 1.00 | 38.3 | 9.2 | 0.32 | 1.9 | 4.0 |
| B0355+508 | 03:59:29.73 | 50:57:50.1 | 150.38 | -1.60 | 30' x 50' | (1.50) ⁶ | 111.3 | 24.2 | 0.30 | 14.3 | 4.2 |
| Mean | | | | | | 0.41 | 17.7 | 6.58 | 0.43 | 2.09 | 1.38 |

¹Sources are placed in three groups according to their discussion in Sect. 3, 4 and 5

²from Schlegel et al. (1998)

³ $N(H I) = 2.6 \times 10^{20} \text{ cm}^{-2} \int \tau(H I) dv$ (see Sect 2) except where noted

⁴ $N(H_2) = N(HCO^+)/3 \times 10^{-9}$ see Sect. 2.

⁵ from Hartmann & Burton (1997), $N(H I) = 1.823 \times 10^{18} \text{ cm}^{-2} \int T_B(H I) dv$
⁶ at such a low galactic latitude E_{B-V} is not reliably determined

⁷ $f_{H_2} = 2N(H_2)/(N(H I) + 2N(H_2))$

OTFUV and SDGRD; the final spatial resolution is 1'. Most maps are approximately 30' × 30' on the sky and were completed in 4-5 hours total observing time. The new CO emission data are presented in terms of the T_R^* scale in use at the 12m antenna and all velocities are referred to the kinematic Local Standard of Rest. The typical rms channel-channel noise in these maps at 1' and 0.26 km s⁻¹ resolution is 0.4-0.5 K; their sensitivity is rather moderate and the detectability limit is of order 1 K km s⁻¹ for a single line component.

More sensitive CO J=1-0 line profiles at higher spectral resolution (25 kHz) had been previously observed toward the continuum sources as part of our survey efforts, for instance see Liszt & Lucas (1998). It is these profiles that are displayed in the Figures shown here representing emission in the specific direction of the background target and used to calculate line profile integrals as quoted in Table 1.

Many interstellar clouds lie at distances of about 150 pc from the Sun, just outside the Local Bubble. At this distance the 1' resolution of our CO mapping corresponds to 0.041 pc.

2.2. H I absorption and emission

The λ 21cm H I absorption spectra shown here are largely from the work of Dickey et al. (1983) augmented by a few spectra taken at the VLA in 2005 May. The spectral resolution of this data is 0.4 - 1.0 km s⁻¹.

Figures B.1 and B.2 of the online Appendix B show latitude-velocity diagrams of H I emission drawn from the Leiden-Dwingeloo Survey of Hartmann & Burton (1997).

2.3. Molecular absorption

Also shown here are spectra of λ 18cm OH absorption from Liszt & Lucas (1996) and mm-wave absorption spectra of CO (Liszt & Lucas, 1998), HCO⁺ (Lucas & Liszt, 1996) C₂H (Lucas & Liszt, 2000) and H₂CO (Liszt et al., 2006).

2.4. Reddening

Maps of reddening were constructed from the results of Schlegel et al. (1998). This dataset has 6' spatial resolution on a 2.5' pixel grid. The stated single-pixel error is a percentage, 16%, of the pixel value. On average, 1 mag of reddening corresponds to a neutral gas column $N(H) = 5.8 \times 10^{21} \text{ cm}^{-2}$ (Savage et al., 1977).

2.5. Target fields

The positions and other observational properties are summarized in Table 1 where the sources are grouped according to their order of presentation in Sect. 3, 4 and 5. The groups appear in order of increasing reddening and gas column density and decreasing distance from the galactic plane. The line profile integrals W_{CO} quoted in Table 1 result from the more sensitive earlier observations noted in Sect. 2.1. The mean values quoted for W_{CO} along individual sightlines are averages over the new map data taken for this work.

Table 2 gives some pixel statistics about noise levels and spatial covering factors as discussed in Sect. 8.

2.6. Presentation of observations

A finding chart including all sources except B1730-130 is shown in Fig. 1 where the locations of the background targets are shown on a large-scale map of reddening, along with locations of a few other landmark objects as noted in the figure caption.

Maps and spectra of the target fields and background sources are shown in Figs. 2-12. Within each of three groups, sources appear in order of increasing right ascension. Members of the first group, shown in Figs. 2-7 and discussed in Sect. 3, are the simplest kinematically. Figs. 8 and 9 show the fields around the background sources B0528+134 and B2200+420 (aka BL Lac) that are also kinematically simple but are heavily patterned and rather bright in CO emission; these are discussed in Sect. 4. Figs. 10-12 (Sect. 5) show the results over three target fields with rather amorphous structure whose kinematics are too complex to fit into the framework in which the data for the other sources are presented in earlier figures. Two of these sources

Table 2. Noise levels and spatial covering factors

| Target | V km s ⁻¹ | σ_{profile} K | σ_{map} K km s ⁻¹ | $f_{>1}^a$ | $f_{>2}^b$ |
|--------|-------------------------|--------------------------------|---|------------|------------|
| B0736 | 5.1,7.2 | 0.43 | 0.48 | 0.18 | 0.07 |
| B0954 | 2.6,5.2 | 0.25 | 0.33 | 0.20 | 0.12 |
| B1730 | 4.0,6.1 | 0.36 | 0.52 | 0.20 | 0.03 |
| B1928 | -4.2,-0.8 | 0.46 | 0.52 | 0.03 | 0.00 |
| B1954 | -1.0,2.4 | 0.33 | 0.35 | 0.20 | 0.13 |
| B2251 | -10.8,-7.9 | 0.28 | 0.32 | 0.06 | 0.02 |
| B0528 | 0.6,3.7 | 0.23 | 0.36 | 0.07 | 0.05 |
| | 8.9,11.7 | | 0.33 | 0.69 | 0.46 |
| B2200 | -3.8,2.8 | 0.39 | 0.63 | 0.61 | 0.50 |
| B0212 | -14.1,-7.9 | 0.30 | 0.80 | 0.26 | 0.11 |
| | -1.4,1.0 | | 0.36 | 0.03 | 0.01 |
| | 1.3,4.9 | | 0.66 | 0.34 | 0.19 |
| B0224 | -17.1,-11.9 | 0.43 | 0.76 | 0.14 | 0.03 |
| | -11.6,-9.2 | | 0.60 | 0.33 | 0.20 |
| | -9.2,-5.1 | | 0.56 | 0.39 | 0.20 |
| | -4.9,-2.0 | | 0.47 | 0.47 | 0.33 |
| | -2.0,-0.2 | | 0.39 | 0.05 | 0.28 |
| | -0.2 .. 2.0 | | 0.42 | 0.09 | 0.03 |
| B0355 | -19.2,-15.9 | 0.35 | 0.63 | 0.18 | 0.07 |
| | -15.8,-11.7 | | 0.92 | 0.43 | 0.28 |
| | -11.1,-9.8 | | 0.59 | 0.34 | 0.18 |
| | -9.6,-7.3 | | 0.62 | 0.34 | 0.10 |
| | -6.0,-1.4 | | 0.79 | 0.17 | 0.04 |

^a fraction of mapped area with $W_{\text{CO}} \geq 1$ K km s⁻¹
^b fraction of mapped area with $W_{\text{CO}} \geq 2$ K km s⁻¹

(B0212+735 and B0224+671) are relatively near each other on the sky and sample similar galactic structure while the third target B0355+508 (aka NRAO150) is the only source within 2° of the galactic equator (see Table 1).

The format of Figures 2-11 is: at upper left a 90' map of $E_{\text{B-V}}$ from the dataset of Schlegel et al. (1998), with an inset showing the field of view mapped in CO, typically 30' on a side; at lower left a map of W_{CO} ; at lower right various atomic (H I) and molecular absorption spectra showing the kinematic structure toward the background source; at upper right, CO emission spectra of various sorts as depicted in the figure captions. The absorption spectra shown at lower right in these figures are somewhat inhomogeneous because not all sources have the same full complement of profiles. In general, H I is at the bottom wherever possible and above that are spectra of the most common molecules observed in absorption; HCO⁺, observed toward all targets, OH, C₂H and/or CO. The uppermost spectrum wherever possible is a species like H₂CO or HNC (Liszt et al., 2006; Liszt & Lucas, 2001) that is detected less commonly and is indicative of greater chemical complexity.

Also shown for all sources are CO emission spectra at various locations in the field mapped, as indicated in the spectra. More complex aspects of the presentation are discussed in the individual figure captions.

2.7. Molecular gas properties in the current sample

The sightlines studied here were selected on the basis of their known HCO⁺ absorption spectra, creating the possibility that the sample is biased to large molecular fractions and/or strong CO emission. However, it was earlier noticed in a flux-limited survey (Lucas & Liszt, 1996) not based on prior knowledge of CO emission that very nearly all sightlines at galactic latitudes within about 15° of the galactic equator show HCO⁺ absorption. Our

present tally, slightly extending the earlier result, is that HCO⁺ absorption occurs toward 19 of 19 sources at $|b| \lesssim 12^\circ$, toward 22 of 25 sources at $|b| \lesssim 18^\circ$ and toward 4 out of 12 sources at $|b| \geq 23^\circ$ including three shown here. Thus it is a near certainty that HCO⁺ absorption would be detected over the entirety of the sky fields mapped here below about 15°-18°, no matter what is the covering factor of detectable CO emission. This is discussed in Sect. 8 immediately following the more descriptive portions of the text.

If we discuss the mean properties of the ten sightlines in Table 1 having reliably determined $E_{\text{B-V}}$ (all except B0355+508 that lies too near the galactic plane) in the same terms that we used earlier to derive the mean CO-H₂ conversion factor in diffuse gas, (Liszt et al., 2010), we derive an ensemble average

$$\begin{aligned} \frac{N(\text{H}_2)}{W_{\text{CO}}} &= \frac{5.8 \times 10^{21} \text{ cm}^{-2} \langle E_{\text{B-V}} \rangle - \langle N(\text{H I}) \rangle}{\langle 2W_{\text{CO}} \rangle} \\ &= 1.52 \times 10^{20} \text{ cm}^{-2} (\text{K km s}^{-1})^{-1}, \end{aligned}$$

i.e., 25% smaller than the previous result found a larger sample. In the same terms, the mean atomic gas fraction is $\langle N(\text{H I}) \rangle / \langle N(\text{H}) \rangle = 0.74$, as opposed to 0.65 found earlier.

Estimates of $N(\text{H}_2)$ based on assuming the ensemble-average mean value (Liszt et al., 2010) $N(\text{HCO}^+)/N(\text{H}_2) = 3 \times 10^{-9}$ along each line of sight are also given in Table 1. They indicate higher molecular fractions and somewhat higher total column densities $N(\text{H})$ than are found using scaled $E_{\text{B-V}}$ for $N(\text{H})$ and using the decomposition discussed just above based on subtracting $N(\text{H I})$ from $N(\text{H})$ determined as the scaled $E_{\text{B-V}}$. Specifically the chemistry-based ensemble average is $\langle f_{\text{H}_2} \rangle = \langle 2N(\text{H}_2) \rangle / \langle N(\text{H I}) + 2N(\text{H}_2) \rangle = 0.43$.

3. Six simple fields at moderate-high latitude

3.1. B0736+0117 ($b \sim 11^\circ$)

The 15' sky field around B0736+016 shown in Fig. 2 is the smallest and kinematically simplest field studied; the map was made on the spur of the moment in a relatively brief open period between two other larger maps. The reddening is modest over the area of the CO map shown in Fig. 2, $E_{\text{B-V}} \lesssim 0.165$ mag but the molecular fraction implied by the entries in Table 1 is of order 30-50%. Toward the source the integrated CO is fairly weak, < 0.8 K km s⁻¹ but a very slightly blue-shifted 4.5 K line is found within just a few arcminutes.

3.2. B0954+658 ($b \sim 43^\circ$)

This source (Fig. 3) is seen at the upper tip of the Polaris Flare near the location of the M81 group and the so-called small area molecular structures mapped by Heithausen (2004) (see the finding chart in Fig. 1). As toward B0736+017, a fairly strong CO line, 5 K, is seen within a few arcminutes of the background target where the CO brightness is more modest, 2 K.

The reddening is very moderate but a high molecular fraction, above 50%, is suggested by comparing the value of $N(\text{H}_2)$ in Table 1 with $N(\text{H I})$ or $E_{\text{B-V}}$. Consistent with this high molecular fraction and the relative simplicity of a higher-latitude line of sight, this field is the only one studied in which there is a strong proportionality between $E_{\text{B-V}}$ and W_{CO} , as discussed in Sect. 8. The complement of supporting material is disappointingly slender.

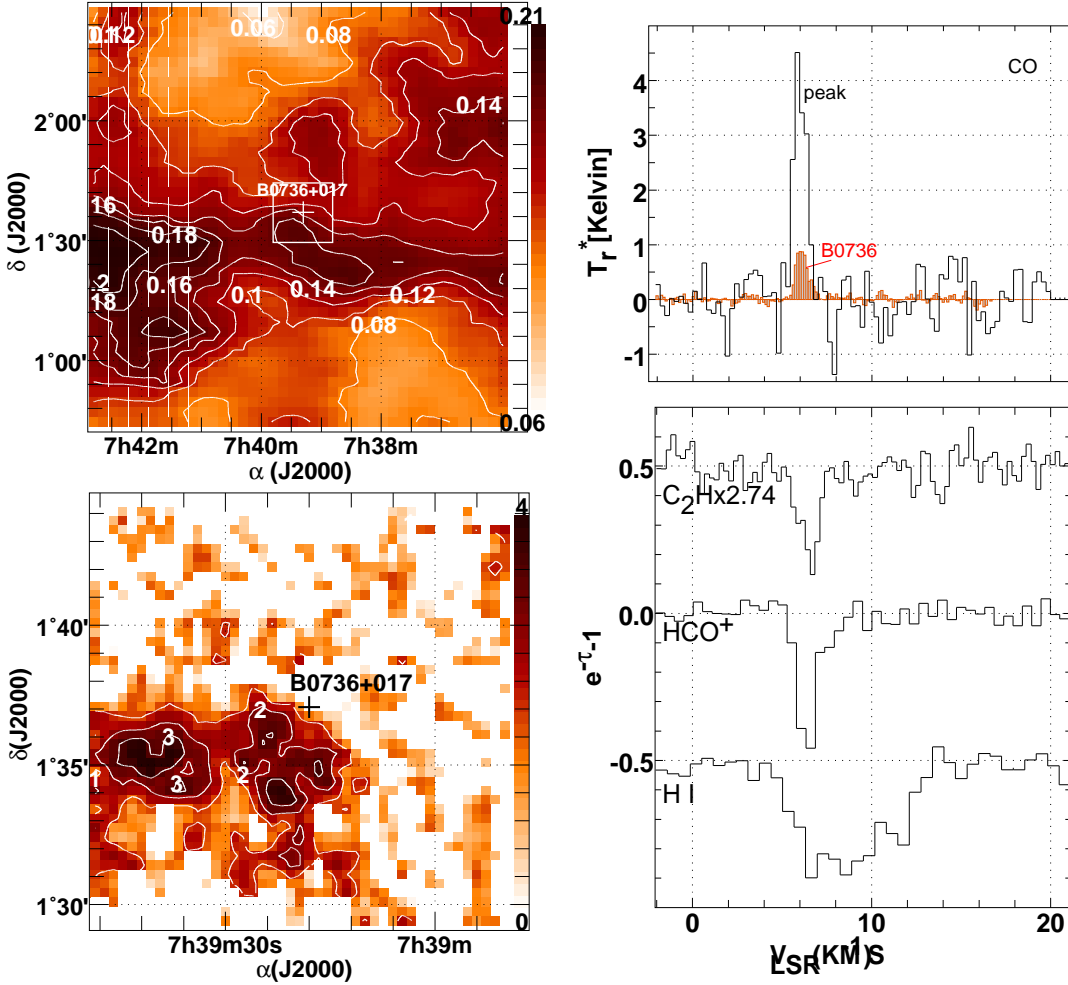


Fig. 2. The sky field around the position of B0736+017. Upper left: reddening at 6' resolution (Schlegel et al., 1998). Lower left: integrated CO emission W_{CO} in units of K km s^{-1} ; contour levels are in 1,2,... K km s^{-1} . Lower right: absorption line profiles, scaled as noted. Upper right: CO emission, toward B0736+017 and at the peak of the nearby CO distribution.

3.3. B1730-130 ($b \sim 11^\circ$)

The reddening is relatively large over this field (Fig. 4) and the HCO^+ absorption is strong, implying a molecular fraction of order one-third, but CO emission is very weak toward the background continuum source ($W_{\text{CO}} = 0.4 \text{ K km s}^{-1}$) and absent over most of the field mapped. Much stronger but still rather weak emission (1.5 K) is seen 15' to the northwest as indicated in Fig. 4. All of the absorption profiles shown in Fig. 4 have a redward wing that is separately visible in the two spatially-averaged CO profiles shown at upper right.

3.4. B1928+738 ($b \sim 23.5^\circ$)

CO emission is absent over the entire 20' field shown in Fig. 5 despite the presence of fairly strong HCO^+ absorption and a suggested molecular fraction approaching 40%. The reddening is modest, approximately 0.15 mag around the target, but the implied CO- H_2 conversion factor is very large; from the entries in Table 1 we have $N(\text{H}_2)/W_{\text{CO}} > 2.5 \times 10^{21} \text{ cm}^{-2}$ at the 2σ level.

3.5. B1954+513 ($b \sim 12^\circ$)

The reddening in the field around this source is modest, 0.18 mag (see Fig. 6 and 17), and CO emission toward the background continuum source is unimpressive (2 K) but the HCO^+ absorption is strong and the molecular fraction is of order 40%. Two kinematic components are found in the field with 4.5 K peak brightness, only one of which is seen toward B1954 in either emission or absorption.

3.6. B2251+158, aka 3C454.3 ($b \sim -38^\circ$)

As shown in Fig. 1, this very strong continuum source is seen about 3° removed from an elongated complex of high-latitude clouds that includes the objects MBM 53-55 (Magnani et al., 1985) and new clouds discovered by Yamamoto et al. (2003). B2251+158 lies within the region surveyed by Yamamoto et al. (2003) in CO but the emission detected here (see Fig. 7) escaped their notice, presumably because of their 4' map sampling of the 2.7' beam. The reddening is moderate, $E_{B-V} \leq 0.11$ mag (see Fig. 7) and CO emission toward the continuum source is quite weak (0.8 K). However, much stronger emission (5 K) is seen only 5' away, as with B0736, B0954 and B1954. There is no obvious large-scale correlation of the CO emission with reddening, as evidenced by the weakness of the CO at the position of highest

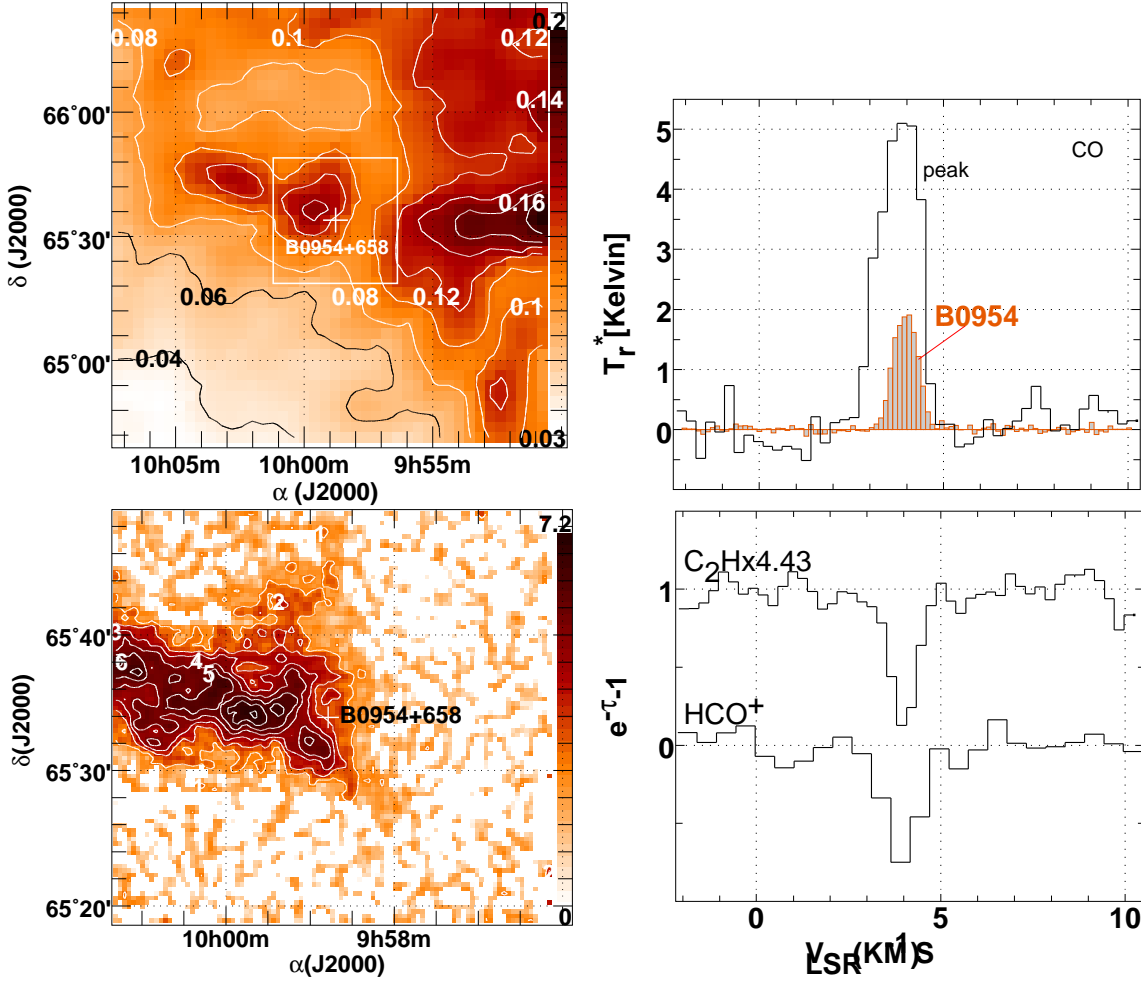


Fig. 3. The sky field around the position of B0954+658, as in Fig. 2.

reddening in the larger field shown at upper left in Fig. 7 (i.e. the spectrum labelled “NW” at upper right there). The relationship between W_{CO} and $E_{\text{B-V}}$ is shown in Figs. 16-17.

The blue wing of the peak emission and the line seen at the northwest reddening peak both fall to the blue of the CO emission or absorption seen toward B2251. Nonetheless they overlap a weaker blue wing of the HCO^+ absorption that has no counterpart in CO emission, and they fill in a portion of the H I absorption spectrum.

4. Two unusual fields at moderate latitude

4.1. B0528+134 ($b \sim -11^\circ$)

Mm-wave absorption toward B0528+134 (Fig. 8) was first discussed by Hogerheijde et al. (1995). This object is viewed against the outer edge of the dark cloud B30 in the λ Orionis ring of molecular clouds (Maddalena & Morris, 1987) that is centered on the H II region S264 and its central ionizing star Lambda Ori (Fig. 1). There is a very substantial foreground reddening $E_{\text{B-V}} = 0.86$ mag and much more heavily extinguished regions in the field to the South.

Although CO emission toward B0528+134 is fairly weak, 2.3 K, emission over the surrounding field is characterized by a pronounced quasi-periodic pattern with some very strong (10-12K) and narrow CO emission lines: emission is undetectable over much of the intervening troughs. A similar wavelike pat-

tern may have been observed across the surface of the Orion molecular cloud by Berné et al. (2010).

A weak blue-shifted component of HCO^+ absorption that is absent in CO toward B0528 has a very bright CO emission counterpart to the Southeast as shown in Fig. 8. Despite an 8 km s^{-1} velocity difference, the blueshifted emission line gives the strong visual impression of being physically associated with the main kinematic component at 10 km s^{-1} , see the map at lower left in Fig. 8. The kinematic span of the CO emission seen at top right in Fig. 8 neatly coincides with the extent of the H I absorption toward B0528+134. Line kinematics in this field are illustrated in more detail in Fig. 14.

4.2. B2200+420 aka BL Lac ($b \sim -10.5^\circ$)

This target (see Fig. 9) was the first source seen in mm-wave absorption from diffuse gas (Marscher et al., 1991), in CO actually, and was also the first seen in HCO^+ absorption in our work (Lucas & Liszt, 1993). CO emission toward the source is fairly strong, 4 K or 6 K km s^{-1} and the line is quite opaque. The molecular column density indicated by the strong HCO^+ absorption is about as large as $N(\text{H})$ inferred from $E_{\text{B-V}} = 0.32$ mag, given the $E_{\text{B-V}}-N(\text{H})$ relationship $N(\text{H}) = 5.8 \times 10^{21} \text{ cm}^{-2} E_{\text{B-V}}$ of Savage et al. (1977).

The CO emission in this field originates from an unusual filamentary morphology (Fig. 9 at lower left) at the edge of an arched pattern in the reddening map. The integrated intensity

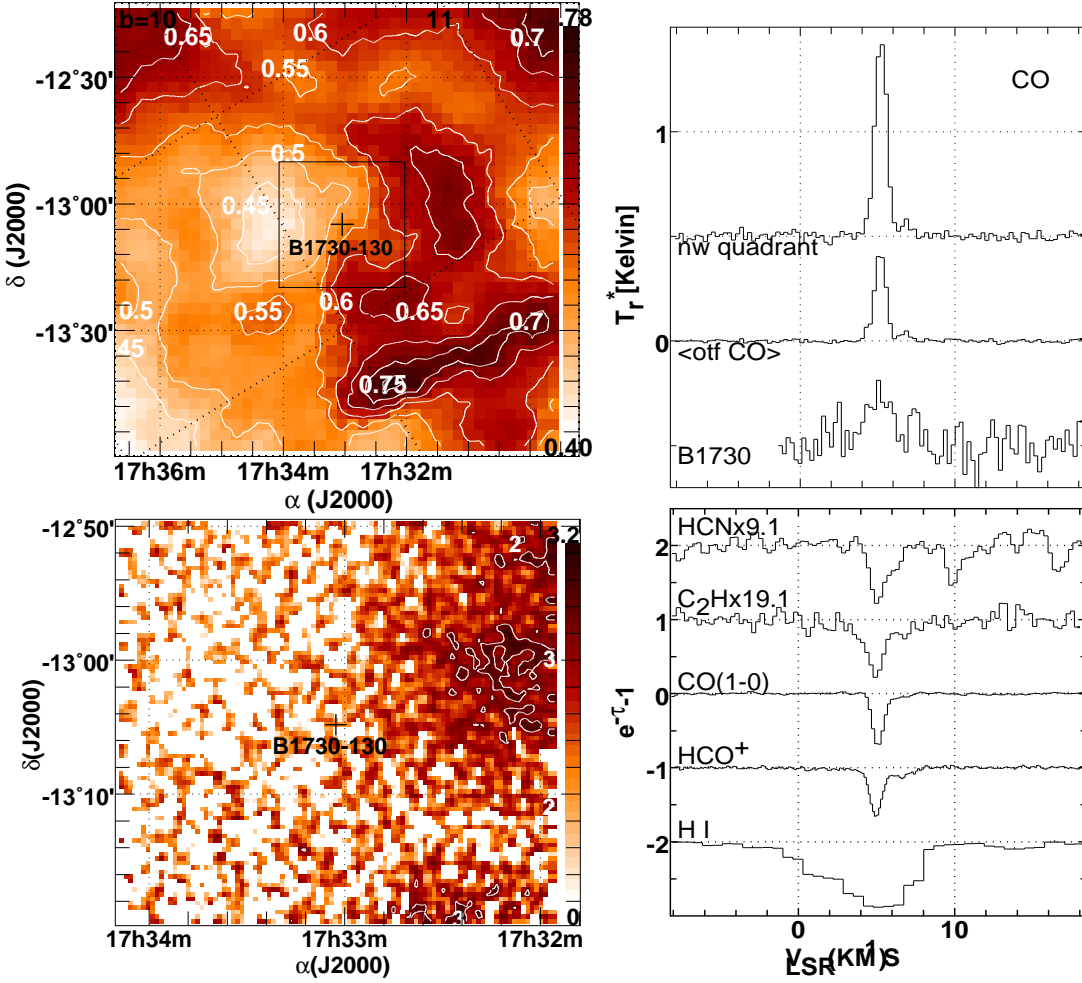


Fig. 4. The sky field around the position of B1730-130, as in Fig. 2. The emission profile labelled “nw quadrant” is an average over that portion of the map. The emission profile labelled $\langle \text{off CO} \rangle$ is the mean over the entire region mapped in CO.

takes on very large values within the field, up to 20 K km s^{-1} but the profile is compound and relatively broad. Toward the continuum source only the blue side of the core of H I absorption is seen strongly in molecular absorption or CO emission but a redshifted CO emission component overlaying the red side of the H I line core is present to the Northeast as indicated in Fig 9.

5. Three complex fields at low-moderate latitude

5.1. B0212+735 ($b \sim 12^\circ$)

B0212+735 (Fig. 10) sits in a mild trough with $E_{B-V} \approx 0.76$ mag in a region of substantial reddening at moderate galactic latitude $b=12^\circ$. It has three molecular absorption components whose balance is entirely opposite to that of H I. Whereas most of the atomic absorption toward B0212+725 occurs in a deep and broad feature at $v \lesssim 10 \text{ km s}^{-1}$, most of the molecules are concentrated in a narrower-lined feature at $v \approx 4 \text{ km s}^{-1}$. An obvious molecular absorption feature at 0-velocity is, very unusually, not apparent in H I. It seems possible that the low velocity resolution of the H I profile (1 km s^{-1}) is responsible. The only other published example of this phenomenon is toward B0727-115 (Lequeux et al., 1993).

The CO emission line kinematics have been color coded at lower left in Fig. 10 to display the observed behaviour in one panel. The gray-scale background represents the integrated in-

tensity of the gas at $1.5\text{-}5 \text{ km s}^{-1}$; higher resolution mapping with the IRAM 30m telescope to be discussed in a forthcoming paper indicates that the feature is compound but this is not apparent in the present dataset. The blue contours represent the CO profile integral at $-16 \text{ km s}^{-1} \leq v \leq -9.5 \text{ km s}^{-1}$; consistent with the prominence of this gas in H I, it is almost as widely distributed over the field as the stronger emission at $1.5\text{-}5 \text{ km s}^{-1}$ (Table 2: 26% vs. 34%) even if it is barely seen toward the continuum. The profile labelled ‘A’ at upper right is an example. The black contours represent the profile integral at $-2 \text{ km s}^{-1} \leq v \leq 1 \text{ km s}^{-1}$ and an example is shown at upper right as profile ‘B’. Emission from this gas occurs only at the eastern edge of the map area.

5.2. B0224+671 ($b \sim 6^\circ$)

This line of sight toward B0224+671 (Fig. 11) samples the two lower-velocity features seen toward B0212+735 but at substantially lower galactic latitude $b=6.2^\circ$, see Table 1. The extinction is large in this field as are the H I and inferred H_2 column densities. CO emission is weak on a per-component basis toward the continuum target but fairly total large values of W_{CO} are attained overall.

The integrated CO emission is compact but rather formless because it is the sum of many kinematic components. Paradoxically, the strongest molecular features seen toward and near B0224+671 are not widely distributed over the map area

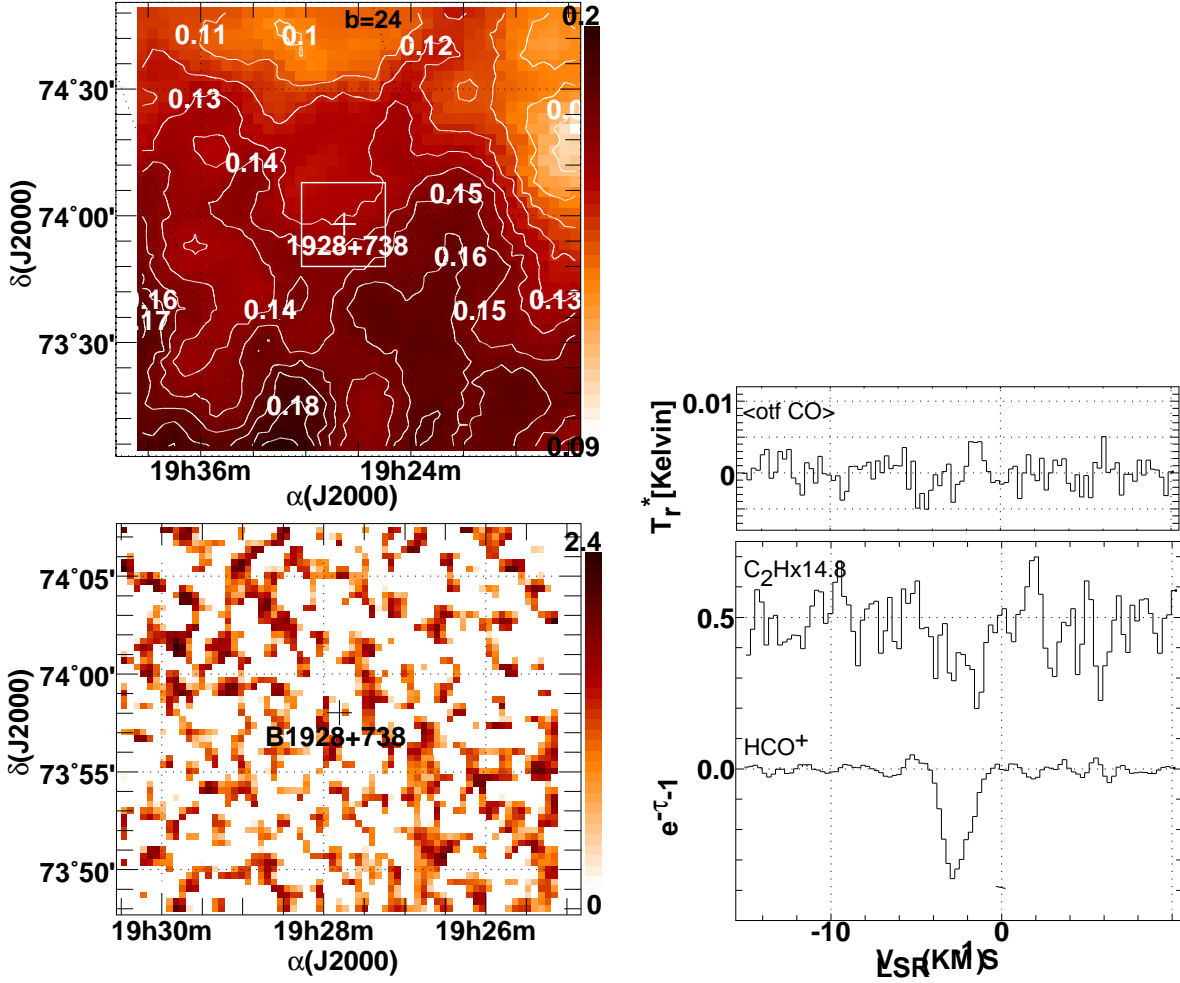


Fig. 5. The sky field around B1928+738. The emission profile at upper right labeled $\langle \text{otf CO} \rangle$ is the mean over the $20' \times 20'$ region mapped in CO.

as shown in the middle panel at right in Fig. 11 comparing the profile toward B0224+671 with the unweighted average of all profiles denoted $\langle \text{otf} \rangle$: the strongest emission peak, at the red edge of the CO emission profile toward B0212+735 is strongly underrepresented in the mean profile. Examples of profiles seen over the map area are shown at upper right in Fig. 11; they were chosen at local peaks in more finely-divided (in velocity) moment maps, with velocity increasing from a to g. Especially at $v < 0 \text{ km s}^{-1}$ the lines shown are much stronger than seen toward the continuum. Among them, the various CO emission components cover the range of strong H I absorption toward the continuum source, $-15 \text{ km s}^{-1} \leq v \leq 2 \text{ km s}^{-1}$. B0224 and B0212 have similar absorption spectra in that both have stronger atomic absorption at $v < -10 \text{ km s}^{-1}$ where the molecular absorption is weaker. They thus sample the same large-scale gas kinematics although they are separated by about 15 pc, assuming they lie on a sphere of 150 pc radius.

5.3. B0355+508 aka NRAO150 ($b \sim -1.6^\circ$)

This is the only low-latitude source studied here. The more strongly blue-shifted gas seen in this direction is likely to be relatively distant. The actual velocity field is probably affected by galactic streaming motions but a typical velocity gradient due to galactic rotation in this direction is $8 \text{ km s}^{-1} \text{ kpc}^{-1}$.

Fig. 12 does not display a map of the reddening for this source because the reddening maps are not believed to be accurate at such low galactic latitudes. Taken as a whole the line of sight is very heavily extinguished, with large columns of both H I and H_2 (Table 1). However, the high inferred H_2 column density is the sum of components whose individual values indicate that they have $A_V \approx 1 \text{ mag}$.

The absorption profiles toward B0355+508 at lower right in Fig. 12 show five obvious HCO^+ and CO components having roughly equal $N(\text{HCO}^+) \approx 1.2 \times 10^{12} \text{ cm}^{-2}$ and somewhat more variable $N(\text{CO})$ (Liszt & Lucas, 1998). Only two have substantial abundances of less-common species such as HCN. Less obvious is the fact that the HCO^+ absorption profile has a weak broad blue wing extending to -35 km s^{-1} so that the entire core of the H I absorption line is seen in molecular gas (see Liszt & Lucas, 2000).

Shown at the top in Fig. 12 are CO moment maps made over velocity intervals corresponding to the obvious HCO^+ and CO absorption line features; a map integrated over all velocities is shown in the top right-most panel. The CO emission distribution is heavily structured and very complex. Profiles at positions of local peaks in narrower CO moment maps are shown at lower left, along with profiles at the integrated emission peak (see Fig. 12 at top right) and toward the background source. At the eastern edge of the map at position “a” there is a blue-shifted CO emission line that (unusually) falls outside the range of the strong

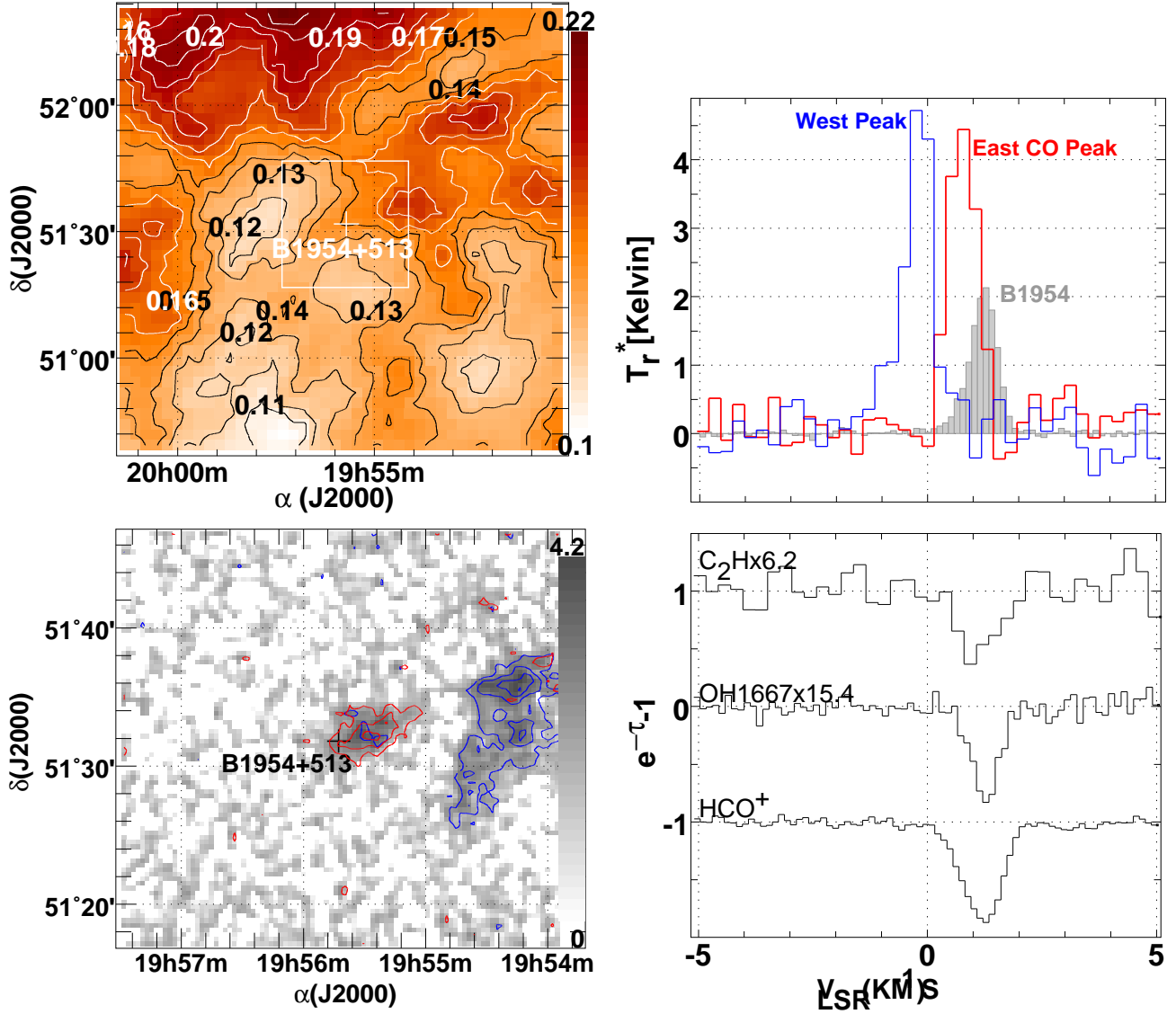


Fig. 6. The sky field around the position of B1954+513, as in Fig. 2. In the map at lower left the grayscale represents the total integrated emission at $-1 \leq v \leq 2 \text{ km s}^{-1}$ and the red and blue contours show the individual distributions of red and blue-shifted components, respectively. Profiles at the peak of the red and blue-shifted emission components are shown at upper right along with the profile toward the continuum source (shaded).

molecular absorption toward B0355+508 but is well inside the H I absorption profile). A very bright ($> 10 \text{ K}$) line is found at $v = -4.5 \text{ km s}^{-1}$ at the northern edge of the map at position f, corresponding to a prominent molecular absorption feature that has only a very weak emission counterpart toward the continuum.

The middle right panel displays the profile toward the continuum background source and the profile averaged over the mapped field of view. The kinematics of this region are shown in more detail in Fig. 15 and discussed in Sect. 7.2. The displacement of the two strong CO emission lines about the centroid of the mean profile results from a coherent kinematic pattern, perhaps a shell or bubble in the underlying gas distribution. Recall, however that absorption at the mean field velocity is not absent toward the continuum source.

The complexity of the emission distribution makes the division into ranges based on HCO^+ absorption quite arbitrary. Moreover, the emission and absorption profiles show rather different structure even toward the continuum target. A very detailed discussion of CO emission within a $90''$ field centered on NRAO150 was given by Pety et al. (2008). Remarkably, the peak

emission brightness seen just $6''$ from the background continuum source is almost 13 K . As the spatial resolution increases, the CO emission profile toward B0355 more nearly resembles the absorption and the blended emission at $v \approx -10 \text{ km s}^{-1}$ resolves into two distinct components.

Conversely, in the present dataset, the emission components seen toward B0355+508 lose their identity as the resolution degrades below a $4'$ hpbw. Both the peak profile and the mean are broad, largely unstructured and centrally peaked about velocities lying between the two strong CO emission components seen toward the background.

6. Statistical lessons

Faute de mieux, the first surveys for suitable absorption-line targets were conducted in CO emission (Bania et al., 1991; Liszt & Wilson, 1993; Liszt, 1994) but the discovery of yet more common HCO^+ absorption (Lucas & Liszt, 1996) caused a reversal in the search strategy for diffuse molecular gas. Thus, all targets studied here were pre-selected to have absorption from HCO^+

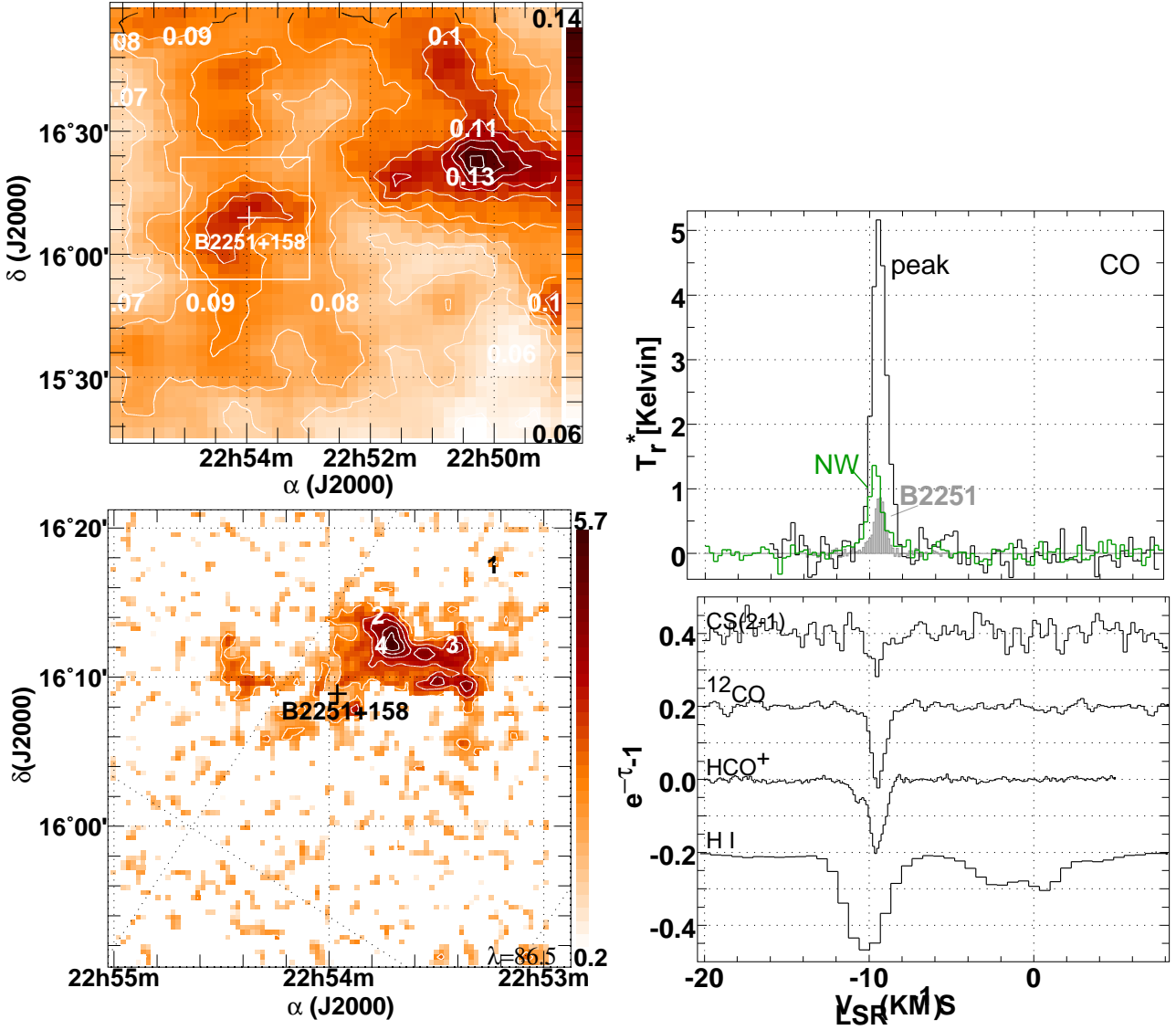


Fig. 7. The sky field around the position of B2251+158 (aka 3C454.3), as in Fig. 2. The map of reddening at upper left is offset to show a separate peak to the Northwest near $22^{\text{h}}50^{\text{m}}$ and a profile at the position of this peak is shown at upper right, shaded green and labeled 'NW', along with profiles toward 3C454.3 (shaded) and at the peak of the small clump that is seen immediately adjacent to the continuum source.

but only some were known to have CO emission. However any division between targets with and without CO emission is misleading because the same sightline may have and lack CO emission on a per-component basis.

Stronger CO emission is always found somewhere else in the map when CO is present toward the continuum but comparably strong CO emission was found, somewhere on the sky, from absorption components lacking CO emission counterparts toward the continuum background. This is true with only one exception, B1928. The implication is that CO emission is somewhat more ubiquitous than is presently believed to be the case because nearly all HCO^+ absorption components will be found in nearby emission after a small search. In terms of numbers, in this work we observed 20 absorption line components (and a few distinct line wings) with 13 carbon monoxide emission counterparts toward the continuum targets, and we found 23 CO emission components within $15'$ of the background continuum source during the mapping.

The following gives some conclusions that are drawn from the preceding presentation; they should generally be understood as applying on a component-by-component basis.

From the standpoint of CO emission:

1) In every case where CO emission was detected toward the background source, much stronger emission was also detected within approximately $15'$ and often much less.

2) Near B0355+508, B0528+134 and B2200+430 the nearby stronger emission was very strong indeed, with peak line temperatures of 10-12 K and/or line profile integrals as large as 20 K km s^{-1} .

3) 1) and 2) are also generally true for kinematic components that were present in absorption toward the continuum source but *not* detected in emission there (7 of 20 components).

4) In one case only (B1928+738), representing 1 of 11 fields and 1 of 20 kinematic absorption line components, the entire field mapped was devoid of emission when emission was not detected toward the continuum source (from a kinematic absorption line component). The field mapped around B1928 was only $20' \times 20'$ as against $30' \times 30'$ or more for all of the other fields.

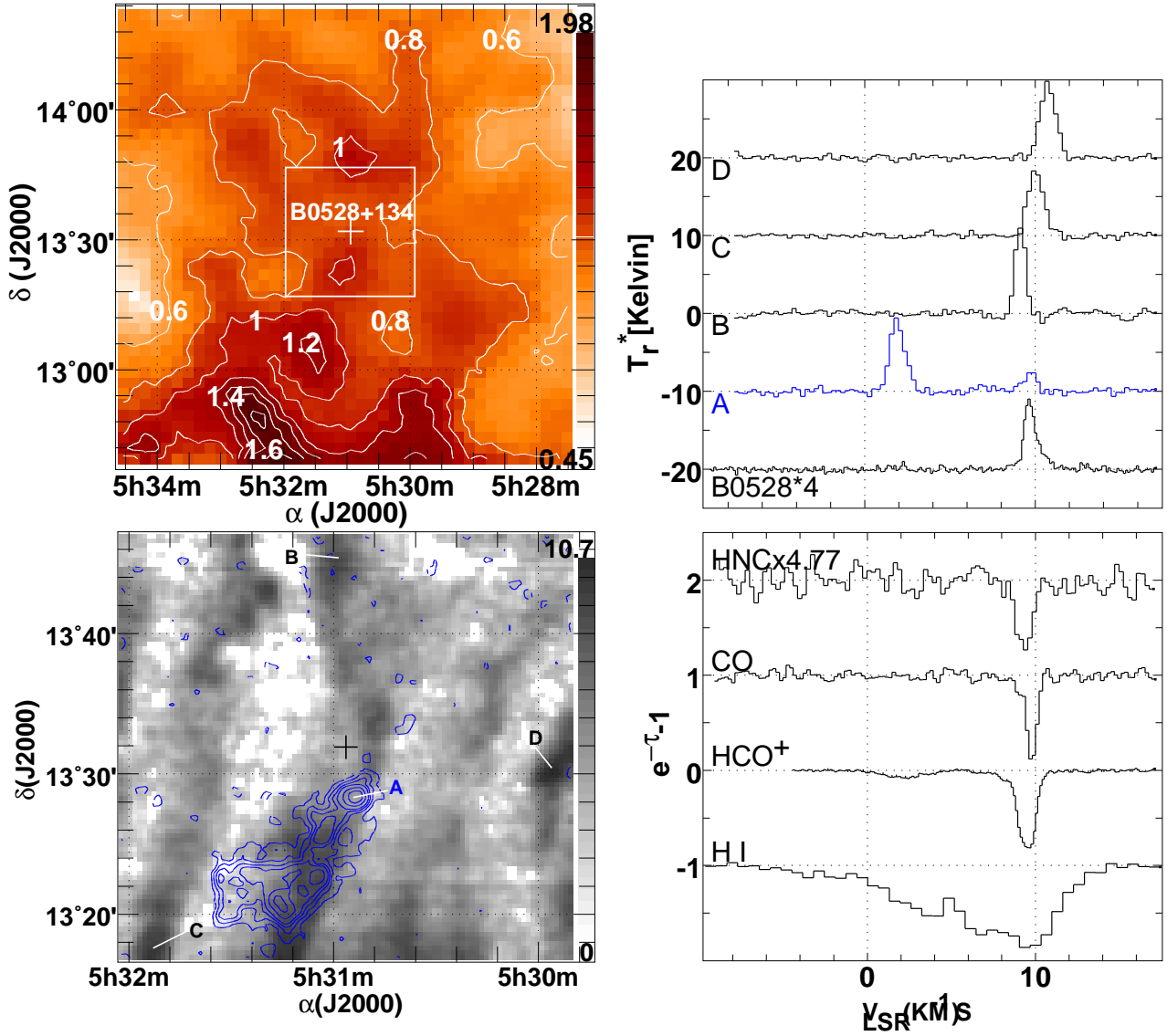


Fig. 8. The sky field around the position of B0528+134, as in Fig. 2. The map of CO emission at lower left superposes the integrated intensity at $0\text{--}4\text{ km s}^{-1}$ as blue contours against a background grayscale representing emission at $v = 8\text{--}12\text{ km s}^{-1}$. Very strong CO lines are seen in the foreground gas as shown in the upper right panel: positions at which they originate are indicated at lower left.

5) In 2 fields we found an emission feature without a counterpart in molecular absorption toward the background continuum object (B1954 and B0355 at -20 km s^{-1}).

From the standpoint of absorption:

1) The same kinematic components are seen in both absorption and emission with angular separations of up to $15'$.

2) The absorption spectra toward a background source are a preview of what will be seen in emission in a larger field about the background source.

3) Molecular absorption components seen toward the continuum source were found in CO emission somewhere in the field except in the smaller region mapped around B1928+738

From the standpoint of the atomic-molecular transition:

1) The same kinematic components are seen in both atomic and molecular tracers at angular separations between $0'$ and $15'$.

2) The components seen in molecular absorption are present in H I absorption, although somewhat indistinctly in some cases. For instance, the 0-velocity molecular absorption line in B0212+735 appears only as a blue wing of the 4 km s^{-1} H I absorption component.

3) Portions of H I absorption profiles adjacent to molecular features but lacking a molecular counterpart are seen in CO emission elsewhere in the field in two cases on (B2200+420 and B0528+134).

4) We saw no molecular features in absorption or emission outside the span of the H I absorption (see Appendix B).

7. Kinematics

Molecular gas is generally well-mixed with other components of the ISM (Dame & Thaddeus, 1994; Gir et al., 1994) and does not require exceptional kinematics. This is apparent in our work from the coincidence of molecular and atomic absorption features, even if they do not have precisely the same patterns of line depth. The kinematics are affected by galactic structure and local external influences such as shocks, but this only becomes apparent on broad angular scales. The targets B0212+735 and B0224+671 (Figs 10-11) are relatively close to each other and both are most strongly absorbed in H I around -15 km s^{-1} . The background target B2251+158 (Fig. 7 and Sect. 3.6) is seen in

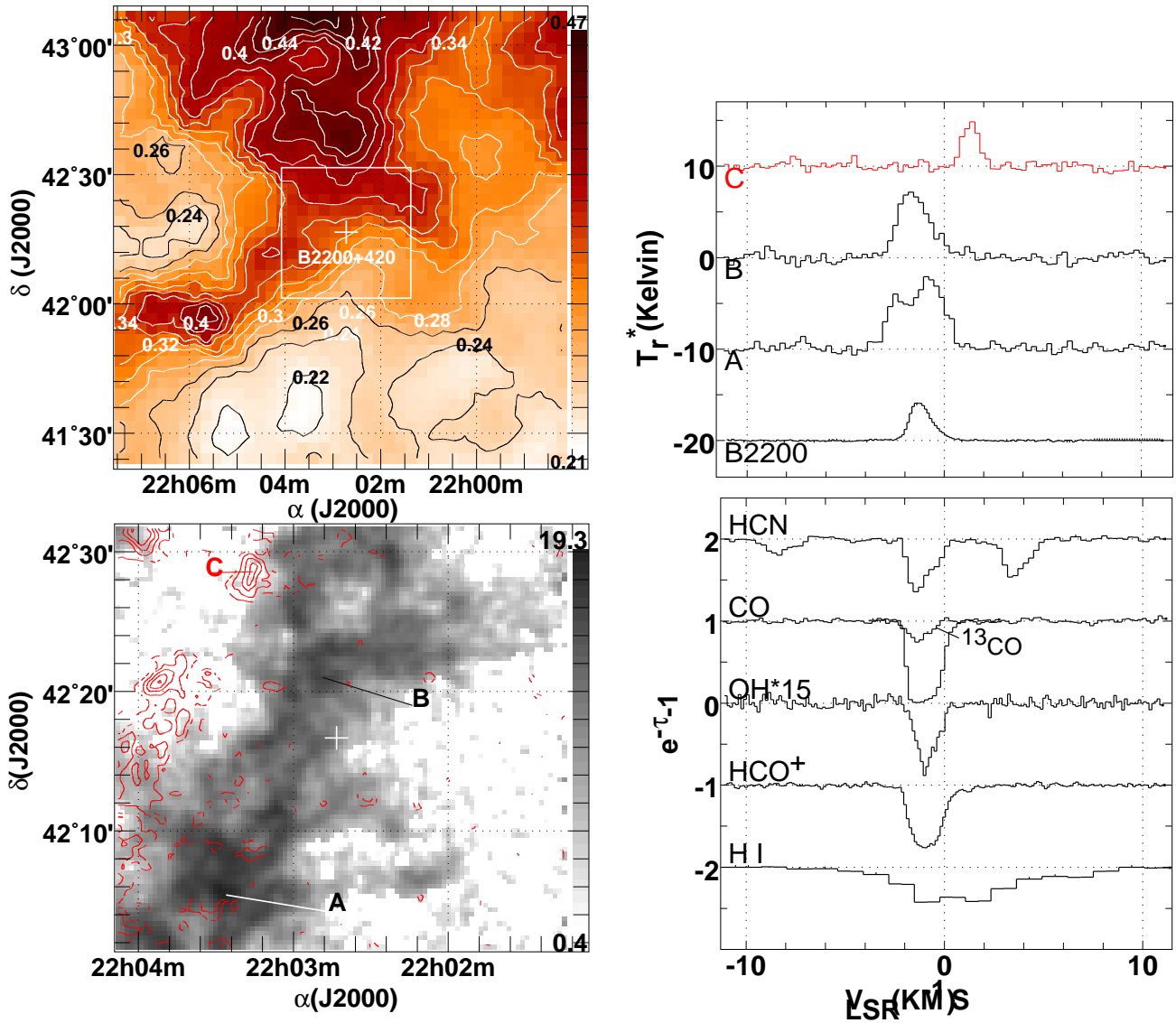


Fig. 9. The sky field around the position of B2200+420 (aka BL Lac), as in Fig. 2. The map of CO emission at lower left superposes the integrated intensity in the range $v=0-2$ km s⁻¹ as red contours against a background grayscale representing the emission at $v \leq 0$ km s⁻¹. Molecular absorption and most emission is sequestered in the blue wing of the core of the HI absorption profile but a red-shifted emission component is present to the Northeast as illustrated by the spectrum at position “C” indicated at lower left.

the outskirts of the MBM53-55 cloud complex, which is part of a large shell that has been extensively mapped in molecular and atomic gas (Gir et al., 1994; Yamamoto et al., 2003).

In individual line profiles and over small scales, the kinematics are often dominated by the internal structure of individual clouds. The internal motions of diffuse molecular gas are now understood to reflect turbulent gas flows (Pety & Falgarone, 2003; Hily-Blant & Falgarone, 2009) that are characterized by unsteady projected velocity fields with strong shears and abrupt reversals of the velocity gradient. Sakamoto & Sunada (2003) show the transition between diffuse and dense molecular gas at the edge of TMC1 and Liszt et al. (2009) discuss gas flows in the diffuse cloud occulting ζ Oph.

In this Section we discuss the kinematics of just two of the fields mapped here. Further examples of CO kinematics in individual sky fields are given in Figs. A.1-A.3 of Appendix A (available online) and the galactic context for all fields is given in Figs. B.1 and B.2 of online Appendix B, showing large-scale latitude-velocity cuts in HI from the Leiden-Dwingeloo HI sur-

vey of Hartmann & Burton (1997) with the locations of the continuum background sources marked in each case.

Fig. 13 shows the kinematics in the relatively simple sky field around B1954+513 (Sect. 3.5 and Fig. 6) with the spatially-displaced blue and red-shifted CO emission components that were illustrated in Fig. 6. The red-shifted component seen toward the continuum has a partially-resolved velocity gradient that carries it just to the midpoint of the associated HCO⁺ absorption profile at the continuum position. It is certain that the blue-shifted CO emission to the East would have an associated HCO⁺ absorption at its position but the structure of the redward gas cannot be traced away from the continuum and, regrettably we do not have an HI absorption profile that might show both the red and blue-shifted gas in atomic absorption as toward BL Lac (Fig. 9 and Sect. 4.2).

Fig. 14 shows the more complicated field at low latitude around B0355+508 (Sect. 5.3, Fig. 12) and illustrates how the partition of a line profile into components, no matter how seemingly obvious, can also be arbitrary and capricious. None of the

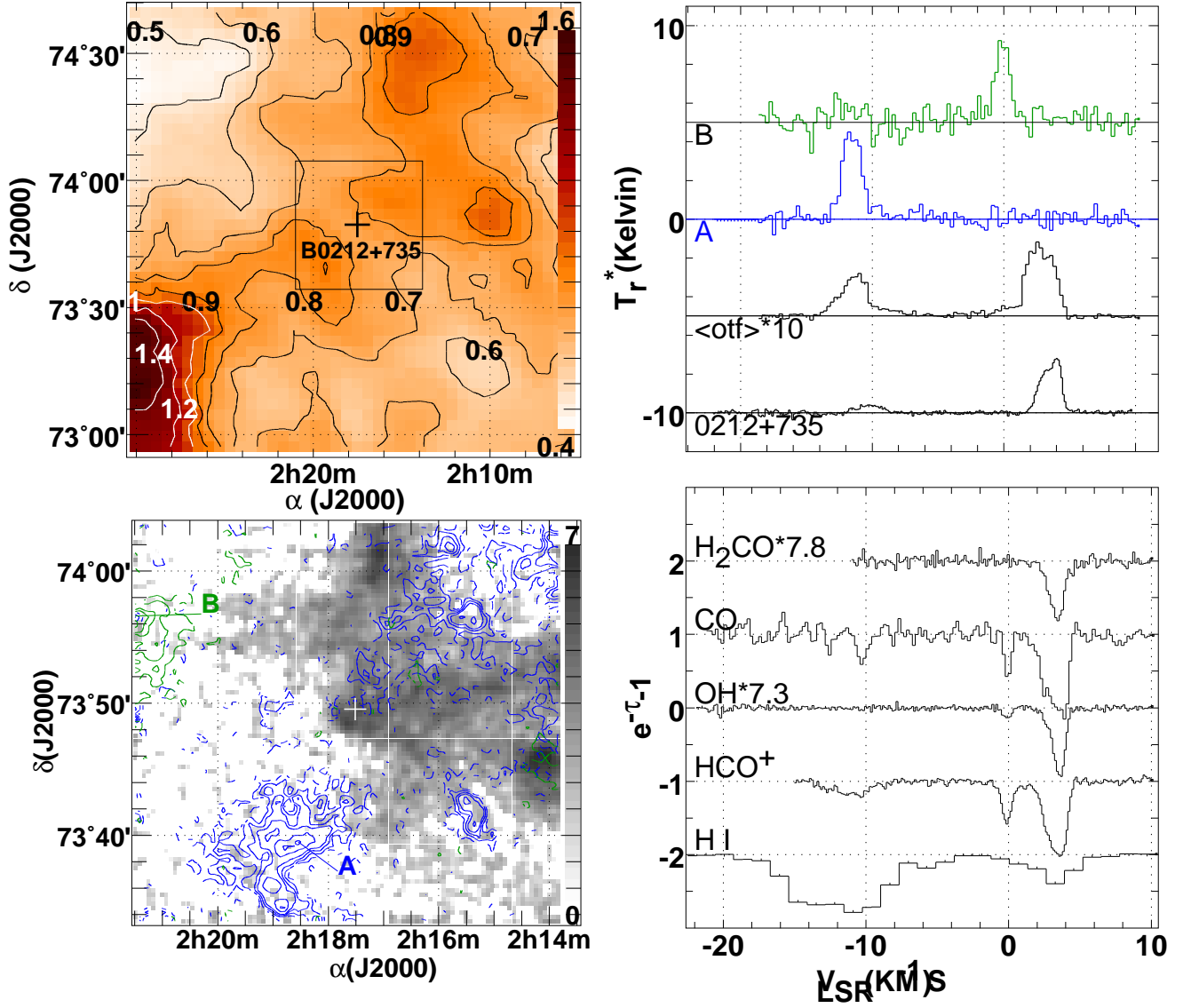


Fig. 10. The sky field around the position of B0212+735, as in Fig. 2. Contours in the CO emission map at lower left are color coded in blue for emission at $-15 \leq v \leq -9.5 \text{ km s}^{-1}$ and in green for emission at $-2 \leq v \leq 1 \text{ km s}^{-1}$. The gray scale background represents the integrated emission of the strongest emission component seen toward the continuum source, at $v = 1.5 - 5 \text{ km s}^{-1}$. ^{12}CO spectra at two locations labelled A and B are shown at upper right along with a strongly-scaled mean profile taken over the full map area.

well-defined absorption features has an obvious CO emission counterpart except perhaps in the immediate vicinity of the continuum target. This is not an artifact of taking a cut in declination, which is actually richer than that in right ascension (see Fig. 12).

Nonetheless, mapping the CO emission does help to clarify interpretation of the absorption profiles. For instance, consider gas near -9 km s^{-1} around the location of B0355 in Fig. 14. In absorption there are two distinct kinematic components at -11 and -8 km s^{-1} that would usually be interpreted as unrelated because, aside from their separation in velocity, they have different patterns of chemical abundances (Fig. 12). However, Fig. 14 shows that the CO emission line has an appreciable velocity gradient across the position of the continuum source, spanning the two absorption lines, making it likely that the two absorption components are part of the same body¹. Moreover, the CO

mapping suggests that the components at -17 and -10 km s^{-1} may also be part of the same structure (and separated by a velocity gradient), which was actually suggested by several coincidences in our earlier high-resolution CO mapping (Pety et al., 2008). The lines at -11 and -17 km s^{-1} are very bright (13 K) at high resolution and have considerable chemical complexity. There are also some seemingly correlated spatial intensity variations. The evidence for an association is entirely indirect but has a clear precedent in the kinematics around B0528+134 (Sect. 4.1 and Fig. 8) where a similar velocity separation occurs between two emission components that are seen superposed in an unusual wave-like spatial configuration.

8. The brightness of diffuse cloud CO

8.1. W_{CO} relative to $E_{\text{B-V}}$ and f_{H_2}

The large-scale finding chart in Fig. 1 is a map of the total intervening gas column density, except where discrete sources of

¹ Pety et al. (2008) show that the overlapping CO emission line is resolved into two kinematic components at $6''$ resolution toward the continuum source.

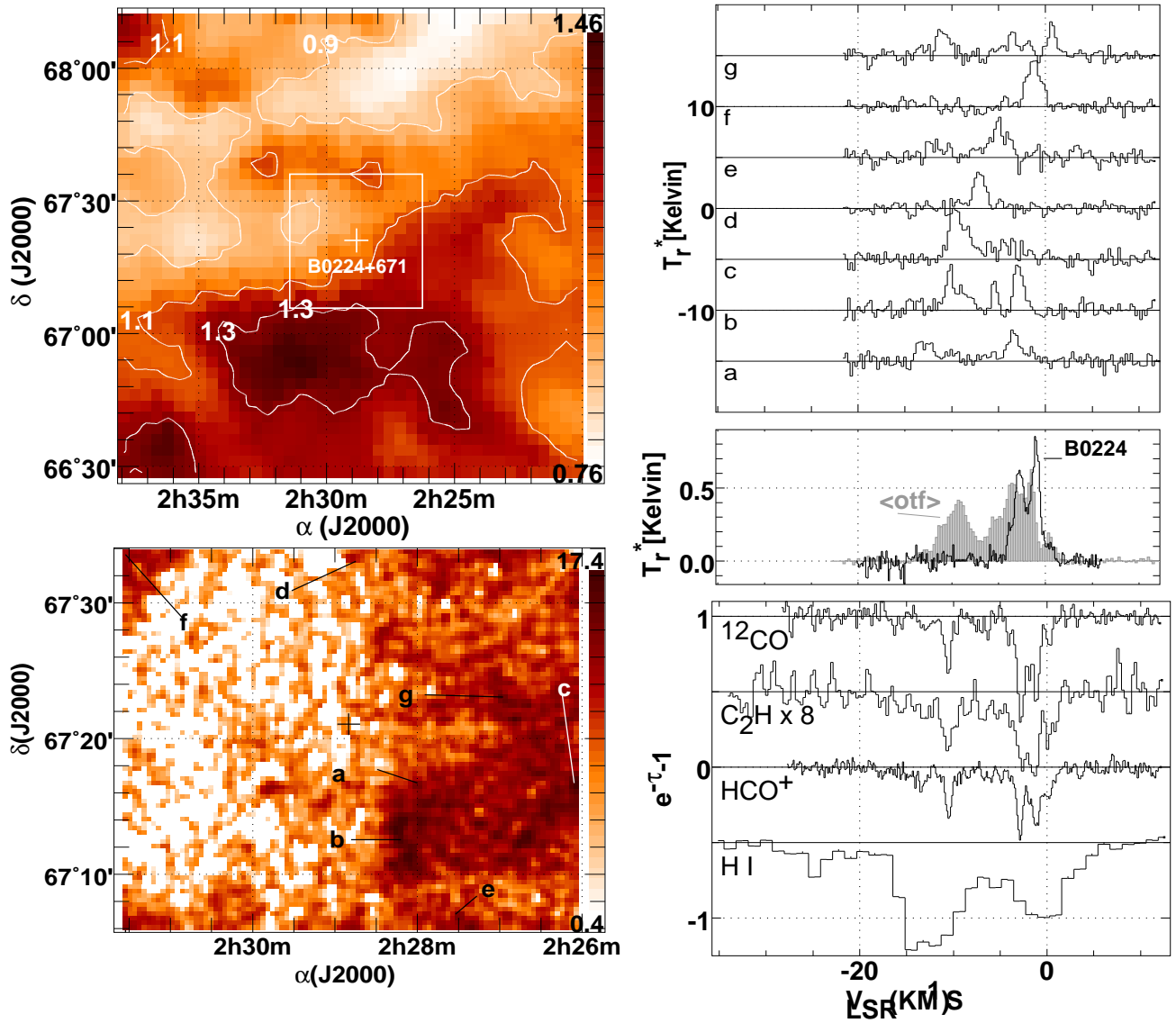


Fig. 11. The sky field around the position of B0224+671, much as in Fig. 2. The map at lower left has been integrated over the very wide interval $-15.5 \leq v \leq +2 \text{ km s}^{-1}$. Shown in the middle panel at right are the CO emission spectrum toward B0224+671 and as averaged over the region of the entire CO emission map. At top right are example profiles from the positions labelled at lower left, chosen from moment maps over narrow intervals increasing in velocity from a-g.

infrared emission (often H II regions) “leak” into the map (usefully indicating when the background target may have been observed through disturbed foreground gas). Large-scale surveys of CO emission at 8’ resolution show a good correlation with reddening (Dame et al., 2001), contributing to the common interpretation of CO sky maps as displaying the global distribution of dense, fully-molecular gas.

In diffuse gas appreciable scatter in the $W_{\text{CO}}\text{-}E_{\text{B-V}}$ relationship is expected because the reddening is a sum over atomic and molecular components that both make important contributions to $N(\text{H})$, combined with the fact that both $N(\text{H}_2)$ and $N(\text{CO})/N(\text{H}_2)$ exhibit order-of-magnitude or larger scatter with respect to $E_{\text{B-V}}$ even when all quantities are measured along the same microscopic sightlines toward nearby bright stars (Burgh et al., 2007; Rachford et al., 2009). The disparity in angular resolution between the reddening data and our 1’ CO maps presents another sort of complication that is considered in Sect. 8.2 but does not by itself dominate the scatter. Recall also the discussion in Liszt et al. (2010) where a good correlation was shown between $E_{\text{B-V}}$

at 6’ resolution compared with the integrated H I optical depth measured in absorption at 21cm toward a larger set of the same kind of point-like radiocontinuum background target considered here.

Small-scale maps of reddening are shown in the various Figs. 2-12 detailing the individual fields. They may visually suggest correlations between $E_{\text{B-V}}$ and W_{CO} , and there is a threshold $E_{\text{B-V}} \geq 0.09$ mag for detecting CO emission, consistent with the well-known and quite abrupt increase of $N(\text{H}_2)/N(\text{H})$ at comparable reddening (Savage et al., 1977). However, reddening is not a reliable predictor of CO emission in our sky fields. For instance, in the field around B2251+158 in Fig. 7, CO emission is much weaker at the peak of the reddening map where $E_{\text{B-V}} = 0.14$ mag (the profile indicated as “NW” at upper right in Fig. 7) than nearer the continuum source at smaller $E_{\text{B-V}} = 0.10$ mag. Around B2200+420 (Fig. 9) the shape of the CO distribution appears to parallel that of the reddening but in detail CO only traces the edge rather than the peak ridge of the $E_{\text{B-V}}$ distribution.

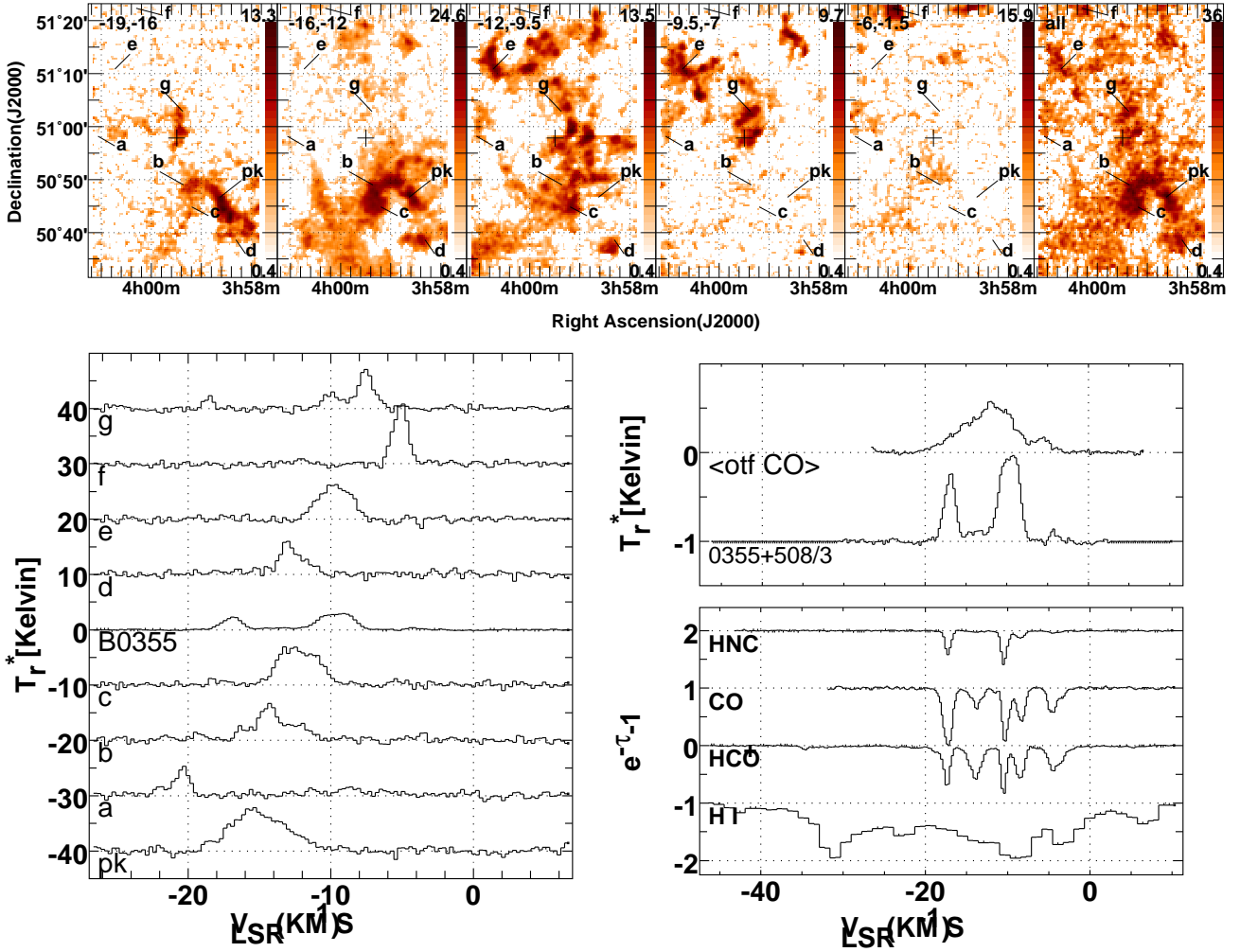


Fig. 12. The sky field around the position of B0355+508. At top are maps of integrated CO intensity made over the velocity intervals indicated in each panel, corresponding to the five strong components of the HCO⁺ absorption profile seen at lower right. CO emission profiles at various locations indicated in the map panels are shown at lower left. CO emission profiles toward B0355+508 and averaged over the map area are shown above the absorption line profiles.

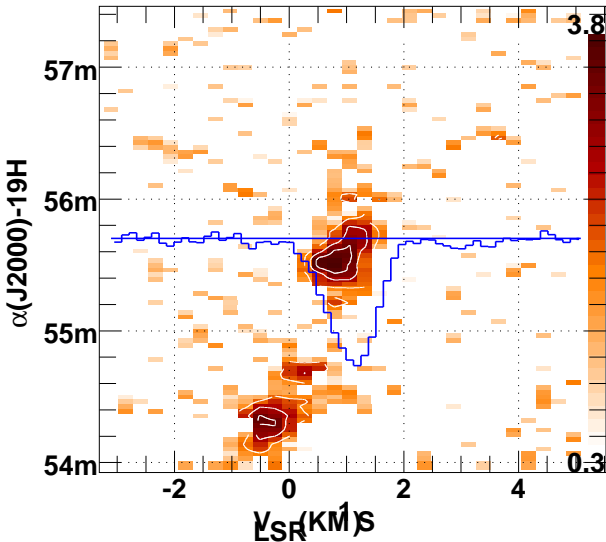


Fig. 13. A right ascension-velocity diagram of CO emission through the position of B1954+513. The HCO⁺ (not CO) absorption spectrum toward B1954 is shown with its 0-level at the location of the continuum source; the peak absorption is 90%. Contours are shown at levels 1, 2, 3, ... K.

In Fig. 15 we show the relationship between W_{CO} and E_{B-V} in the four simple cases discussed in Sect. 3, where the extinction is small and a single narrow CO spectral component is present at each pixel². The rms noise levels in these four datasets (Table 2) are 0.48, 0.33, 0.32 and 0.35 K km s⁻¹ reading clockwise from upper left so that datapoints with $W_{CO} \geq 1$ K km s⁻¹ (the usual last contour on CO sky maps) are detected at or above the 90% confidence level. To put these brightness and sensitivity levels in context, note that there is a straightforward relationship between W_{CO} , f_{H_2} , and E_{B-V} once the CO-H₂ and $E_{B-V}/N(H)$ conversion factors are fixed; for the *standard* $W_{CO}/N(H_2) = 2 \times 10^{20}$ cm⁻² H₂ (km s⁻¹)⁻¹ and $N(H)/E_{B-V} = 5.8 \times 10^{21}$ cm⁻² mag⁻¹ one has $W_{CO} = 14.5 f_{H_2} E_{B-V}$ K km s⁻¹. At $E_{B-V} = 0.1$ mag, emission only slightly exceeding 1 K km s⁻¹ implies a molecular fraction $f_{H_2} > 1$ and therefore is too bright to be accommodated by a CO-H₂ conversion factor as large as the standard 2×10^{20} cm⁻² H₂ (km s⁻¹)⁻¹.

Shown in each panel of Fig. 15 are lines representing the CO emission expected if various fractions f_{H_2} of the total neutral gas column are in H₂ with a typical galactic $W_{CO}/N(H_2)$ conversion factor $X_{CO} = 2 \times 10^{20}$ H₂ cm⁻² (K km s⁻¹)⁻¹. Much of

² Green diamonds in Figs. 15 and 16 show E_{B-V} and W_{CO} toward the continuum target as given in Table 1

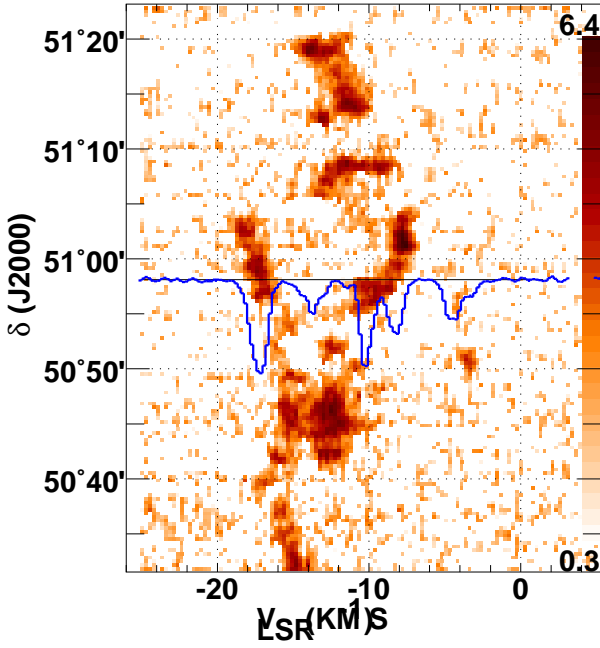


Fig. 14. A declination-velocity diagram of CO emission at the right ascension of B0355+508. The CO absorption spectrum toward B0355+508 is shown with its baseline level at the declination of the background source. The strongest CO absorption line is quite opaque, see Fig. 12.

the CO in Fig. 15 occurs above the line corresponding to $f_{\text{H}_2} = 1$ and is therefore too bright to be accommodated by the usual CO-H₂ conversion factor; indeed, almost every CO line with $W_{\text{CO}} \gtrsim 1 \text{ K km s}^{-1}$ may be described as overly-bright in this way if $f_{\text{H}_2} = 0.5$, hence the great majority of all the statistically significant emission represented in Fig. 15 and in the maps shown earlier for these sources. For the brightest pixels $N(\text{H}_2)/W_{\text{CO}} < 5 \times 10^{19} \text{ H}_2 \text{ cm}^{-2} (\text{K km s}^{-1})^{-1}$.

The same $W_{\text{CO}}-E_{\text{B-V}}$ diagrams are shown for sources with higher $E_{\text{B-V}}$ in Fig. 16. Much of the gas around B2200+420 falls above the line for $f_{\text{H}_2} = 1$, and attains such high brightness that its H_2/W_{CO} ratio is 3-4 times below the standard conversion factor. However, this case becomes increasingly harder to make toward the other sources having higher $E_{\text{B-V}}$ as in the bottom panels of Fig. 16.

8.2. Sub-structure in reddening would not eliminate large $W_{\text{CO}}/E_{\text{B-V}}$ ratios

CO emission is heavily structured on arcminute scales, well below the 6' angular resolution of the reddening maps, and the high values and large scatter in $W_{\text{CO}}/E_{\text{B-V}}$ in Fig. 15 cannot be accommodated with a fixed ratio of $W_{\text{CO}}/N(\text{H}_2)$ or $W_{\text{CO}}/N(\text{H})$ except by positing strong unresolved variations, essentially clumping, in $E_{\text{B-V}}$. It is important to understand the extent to which this might represent unresolved structure in the total column density, for instance with regard to cleaning maps of the cosmic microwave background (Planck Collaboration et al., 2011). Given the extreme sensitivities of the CO abundance and brightness to $N(\text{H}_2)$ in diffuse clouds and the fact that even f_{H_2} may vary in diffuse material, it is entirely possible that the large contrasts seen in W_{CO} do not have strong consequences for the distribution of $N(\text{H})$, $E_{\text{B-V}}$, or even $N(\text{H}_2)$.

Shown in Fig. 17 are cumulative distribution functions of the integrated CO emission W_{CO} in the fields around B0954+658

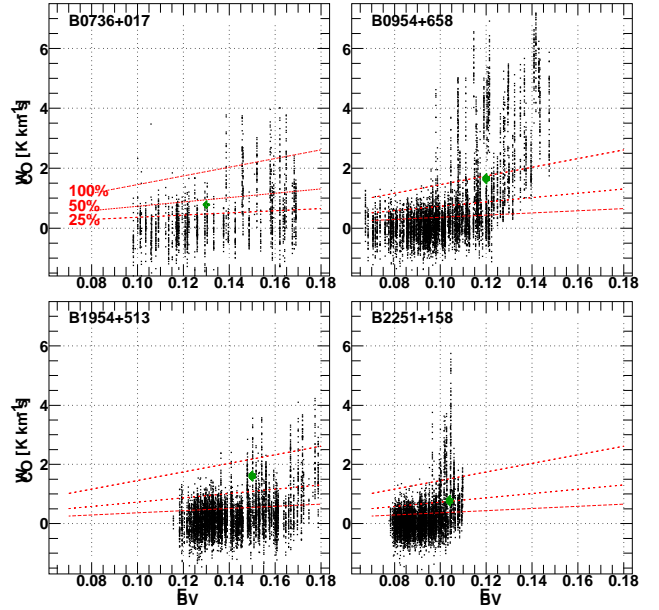


Fig. 15. Distribution of $E_{\text{B-V}}$ and W_{CO} for four fields mapped here in CO. Each 20'' pixel in the CO maps is plotted as a separate point. The (red) dashed lines in each panel show the CO emission expected if 25%, 50% and 100% of the gas is in molecular form with a typical value of the $W_{\text{CO}}-N(\text{H}_2)$ conversion factor, $N(\text{H}_2)/W_{\text{CO}} = 2 \times 10^{20} \text{ H}_2 \text{ cm}^{-2} (\text{K km s}^{-1})^{-1}$. In each panel a (green) filled diamond is shown at the value given in Table 1 toward the background source.

and BL Lac, using the native ARO data and versions of the data smoothed to lower angular resolution 3' (similar to NANTEN) and 5' (similar to Planck). The brightness distribution of the CO around B0954+658 is compact in Fig. 3 but still sufficiently extended that 4.5 K km s^{-1} integrated intensities are present at 5' resolution; this is well above the line for $f_{\text{H}_2} = 1$ in Fig. 15.

The distribution of strongly emitting CO around BL Lac is sufficiently broad in angle that 20-30% of the pixels are occupied by CO with $W_{\text{CO}} \geq 5 \text{ K km s}^{-1}$ whether the angular resolution is 1' or 5'; the very strongest CO lines have $W_{\text{CO}} \gtrsim 15 \text{ K km s}^{-1}$ at 1-5' resolution in the BL Lac field. This is consistent with our recent observations of CO emission in the field around ζ Oph (Liszt et al., 2009) where the same peak brightnesses were found in ARO and NANTEN data at 3' resolution.

Because high CO brightness, and, therefore, impossibly high ratios $W_{\text{CO}}/E_{\text{B-V}}$ (requiring $f_{\text{H}_2} > 1$ for the mean $W_{\text{CO}}/N(\text{H}_2)$ ratio) persist to low angular resolution, W_{CO} cannot maintain a constant proportionality to $N(\text{H}_2)$ over the body of these clouds. The observed variations in W_{CO} are too large to be accommodated by the total amount of material that is present along the line of sight and unresolved structure in reddening cannot account for the high values of $W_{\text{CO}}/E_{\text{B-V}}$ or the range of variation in that ratio.

8.3. Covering factors and bright and dark CO

In Sect. 2.7 we noted the statistical certainty with which HCO^+ absorption is found in spectra taken within about 15° - 18° of the galactic plane. A corollary to this is that molecular gas is certain to be omnipresent over the sky fields mapped in CO at such latitudes, no matter how much of sky we actually found to be occupied by CO emission.

Table 2 shows pixel statistics for the CO emission maps made in the course of this work; shown are profile channel-

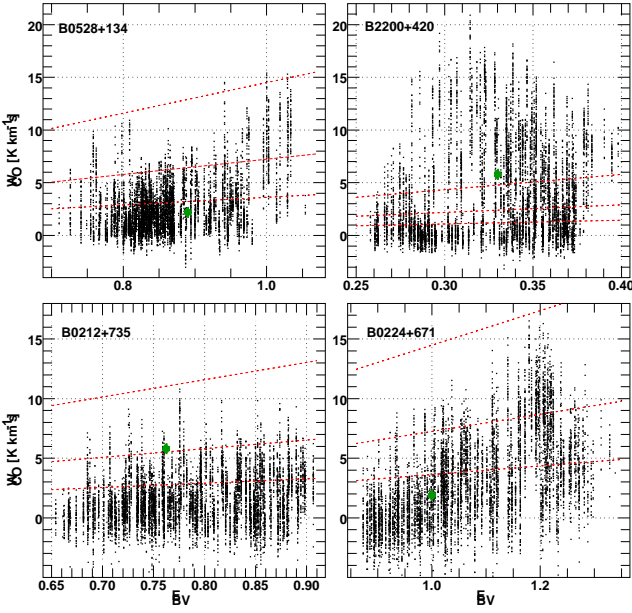


Fig. 16. As in Fig. 15 for four fields with larger reddening.

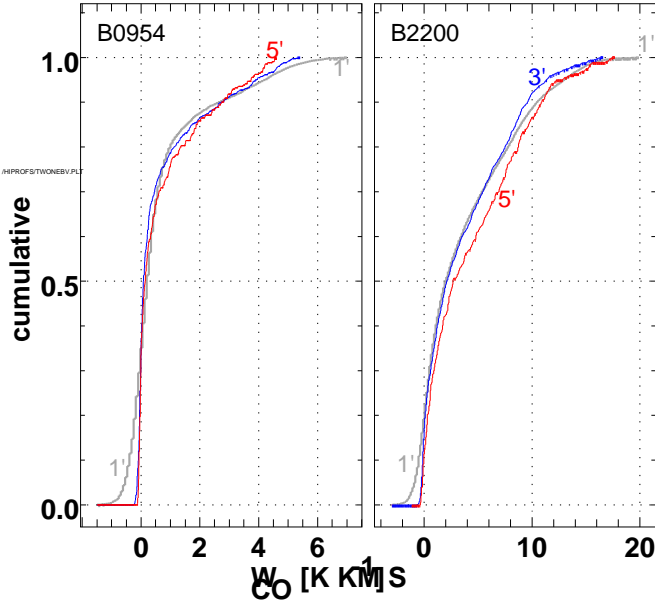


Fig. 17. Cumulative distribution functions for W_{CO} at spatial resolutions of 1' (gray, thicker), 3' (blue) and 5' (red) for B0954 (left) and B2200.

channel rms noise values and map pixel-pixel rms noise in W_{CO} for each mappable kinematic component. In each case the covering factor was determined by forming a histogram of the W_{CO} values and subtracting a gaussian fit to the component corresponding to the noise, and is apparent in that it extends to unphysical negative values of W_{CO} . This is not a large correction; if the noise in W_{CO} is random at a level σ_{map} the covering factor at/above any given W_{CO} in the absence of signal is $dA(W_{\text{CO}})/A = 0.5(1 - \text{erf}(W_{\text{CO}}/\sqrt{2}\sigma_{\text{map}}))$. The expected covering factor due to noise at even 2σ significance is already below 3%.

Table 2 shows that typical covering factors are 20%-40%, with a few null values and only two sky fields (B0528 and B2200) where the majority of the map area is covered. Very approximately, the covering factors are small to about the same extent that the $W_{\text{CO}}/N(\text{H}_2)$ conversion factors of the detected CO emission are higher than indicated by the standard CO- H_2 con-

version. In the end, some form of spatial averaging over brighter and dimmer CO must be responsible for the global mean CO- H_2 conversion factor whether in fully molecular or diffuse molecular gas. The idea that all gas parcels would show identically the same $W_{\text{CO}}/N(\text{H}_2)$ is preposterous.

8.4. Pressure and density in CO-emitting gas

Partial pressures of molecular hydrogen $p(\text{H}_2)/k = n(\text{H}_2)T_K$ were derived by Liszt & Lucas (1998) for all of the CO-bearing clouds discussed here, in the directions of the background targets. They generally fall in the range $1 - 5 \times 10^3 \text{ cm}^{-3} \text{ K}$, typical of thermal pressures in the diffuse ISM sampled by neutral atomic carbon (Jenkins & Tripp, 2011), which should share the same volume. The CO derivation depends on recognizing that, when the gas is warm and excitation is strongly sub-thermal, the excitation temperature of the $J=1-0$ transition depends only on $p(\text{H}_2)$ and the optical depth of the transition $\tau(1-0)$. In the limit of zero optical depth the excitation temperature of the $J=1-0$ transition $T_{\text{exc}}(1-0)$ is only proportional to $p(\text{H}_2)$, not to either the temperature or density independently, making CO a useful barometer. This first became apparent in the work of Smith et al. (1978) and is illustrated in Fig. 11 of Liszt & Lucas (1998): it has persisted over several generations of improved collision cross sections. Moreover, the excitation contribution from atomic hydrogen should be small in CO-bearing gas where the molecular fraction must be appreciable even if H_2 does not dominate the overall atomic-molecular balance (Liszt, 2007).

For $\tau(1-0) \lesssim 3$ and $p(\text{H}_2)/k \lesssim 2 \times 10^4 \text{ cm}^{-3} \text{ K}$ the behaviour seen in Fig. 11 of Liszt & Lucas (1998) may be straightforwardly parameterized to an accuracy of a few per cent as

$$T_{\text{exc}}(1-0) - T_{\text{cmb}} = 0.303K \left[\frac{p(\text{H}_2)}{10^3 \text{ cm}^{-3} \text{ K}} \right]^{1.02} e^{\tau(1-0)^{0.6}/2.6} \quad (1)$$

As examples of the application of this notion, we note:

- For a typical line with $\tau(1-0) = 1.5$ and a Rayleigh-Jeans brightness above the CMB of 1.5 K, $T_{\text{exc}}(1-0) = 5.04 \text{ K}$ and $p(\text{H}_2)/k = 5 \times 10^3 \text{ cm}^{-3} \text{ K}$ or $n(\text{H}_2) = 200 \text{ cm}^{-3}$ at $T_K = 25 \text{ K}$.
- For the strongest absorption line component toward B0355 (-17.8 km s^{-1}), $\tau(1-0) = 3.1$ and $T_{\text{exc}}(1-0) \approx 6 \text{ K}$, so that $p(\text{H}_2)/k \approx 5 \times 10^3 \text{ cm}^{-3} \text{ K}$ once more.
- The $\approx 4.5 \text{ K}$ lines observed at the peak positions in several of the simple fields discussed in Section 3 require $p(\text{H}_2)/k \gtrsim 8.5 \times 10^3 \text{ cm}^{-3} \text{ K}$ or $\gtrsim 15 \times 10^3 \text{ cm}^{-3} \text{ K}$ for $\tau(1-0) = 3$ or 1, respectively. Such a heavy over-pressure must be transient.
- The very bright 10-12 K lines seen near B0528+134 and B2200+420 require excitation temperatures of 15 K or more and lie somewhat beyond the range where W_{CO} and $N(\text{CO})$ can be shown to be linearly proportional. They will be discussed separately in a forthcoming publication based on observations of HCO^+ , HCN , and CS .

8.5. Failing to detect H_2 when CO emission is weak

There are cases where the brightness of the 1-0 line is well below 1 K even when the CO optical depth is appreciable, as summarized in Table 3; unfortunately we do not have a CO absorption profile toward B1928+738 in whose field CO emission was not detected, see Sect. 3.4. The regions of very low $p(\text{H}_2)$ toward B0212 and B0224 somehow manage to produce appreciable amounts of CO without exciting it to detectable levels but

other lines represented in Table 3 do not arise in regions of especially low pressure.

In Sect. 2.7 we showed that, on the whole, molecular gas is not underrepresented by CO emission in the collection of sightlines comprising this work and earlier we showed that the same is true of the larger sample of absorption-cloud sightlines from which the current sample was drawn (Liszt et al., 2010). Moreover, CO emission from all of the components represented in Table 3 is detected (usually quite strongly) elsewhere in the mapped fields except around B1928. However, the fraction of molecular gas that is detectable in CO along individual sightlines varies substantially. To quantify this we equate the molecular column density with the integrated optical depth measured in HCO^+ (Lucas & Liszt, 1996), see the right-most column in Table 3. In this case the fraction of molecular gas that is missed by failing to detect CO emission from particular individual components in four directions is 12% toward B0212, 16% toward B0224, 8% toward B0528+134 and 100% toward B1928. Overall the fraction of molecular gas represented by the weakly-emitting CO summarized in Table 3 is 8% toward B0528, 16% toward B0224, 22% toward B0212, 43% toward B0355 and 100% toward B1730 and B1928.

9. Discussion

Even at $E_{B-V} = 0.1 - 0.3$ mag, the CO emission traced in this work runs the full gamut from undetectable to having brightness comparable to that seen in fully-molecular dark clouds. CO emission may be undetectably weak ($\ll 1\text{K}$) when molecular gas is present in absorption (including that of CO itself) but in other directions it may be so bright that the $N(\text{H}_2)/W_{\text{CO}}$ ratio is 4-5 times smaller than the typical CO- H_2 conversion factor $2 \times 10^{20} \text{ cm}^{-2} (\text{K km s}^{-1})^{-1}$. Under the conditions encountered in diffuse clouds, CO emission is foremost an indicator of the CO chemistry, secondarily an indicator of the rotational excitation (which reflects the partial thermal pressure of H_2) and only peripherally a measure of the underlying hydrogen column density distribution as discussed in Sect. 8. Indeed, the simulations of CO emission from the interstellar medium by Shetty et al. (2011) agree with observations for the dense gas. However, a detailed comparison with our results on the diffuse material shows that the radiative transfer factor is correct but there are up to 4 orders of magnitude difference in $N(\text{H}_2)/N(\text{CO})$. This is linked to the poorly-understood polyatomic chemistry in the diffuse gas (see Shetty et al., 2011, their section 4.3).

The over-arching issues most relevant to diffuse cloud CO emission are three-fold: 1) How it may be identified for what it is, originating in relatively tenuous gas that is unassociated with star formation; 2) Whether it makes a substantial contribution when CO emission is used as a surrogate for $N(\text{H}_2)$ in circumstances where emission contributions from diffuse and dense heavily-shielded gas may be blended; 3) How it is related to the so-called “dark” gas discovered by and FERMI (Abdo et al., 2010) and PLANCK (Planck Collaboration et al., 2011) that is most prominent at moderate extinction where the transition from atomic to molecular gas occurs and is claimed to host 50%-120% of the previously-known CO emitting gas in the solar neighbourhood.

As for the identification of diffuse gas, the $W_{\text{CO}}/W_{13\text{CO}}$ ratio is the most accessible and direct probe. When diffuse cloud CO is excited to detectable levels it is generally in the regime where $W_{\text{CO}} \propto N(\text{CO})$ and $W_{13\text{CO}} \propto N(^{13}\text{CO})$ so that the brightness ratio $W_{\text{CO}}/W_{13\text{CO}}$ will be much larger than the values 3-5 that are seen when emission arises from optically thick lines from denser

gas where the rotation ladder is close to being thermalized. Fractionation progressively lowers the $N(^{12}\text{CO})/N(^{13}\text{CO})$ column density ratio in diffuse gas at larger $N(\text{CO})$ (Liszt & Lucas, 1998; Sheffer et al., 2007) but not below about 15. Intensity ratios $W_{\text{CO}}/W_{13\text{CO}}$ of 8-10 or higher are a strong indicator that there is a major contribution from diffuse material.

Regarding the contribution of diffuse gas we recently assessed it in the case where an outside observer looked down on the Milky Way disk in the vicinity of the Sun (Liszt et al., 2010). We compared the mean emission for the ensemble of lines of sight from which the current background targets were drawn with the vertically-integrated emission expected for the galactic disk component at the Solar Circle drawn from galactic plane surveys. The ensemble mean in our dataset, expressed as an equivalent to looking vertically through the galactic layer, was $2 < W_{\text{CO}} \sin(|b|) > = 0.47 \text{ K km s}^{-1}$. The galactic disk contribution was inferred from galactic plane surveys that find $A(\text{CO}) = 5 \text{ K km s}^{-1} (\text{kpc})^{-1}$ and an equivalent disk thickness of 150 pc, implying an integrated intensity through the disk of $5 \text{ K km s}^{-1} (\text{kpc})^{-1} \times 0.15 \text{ kpc} = 0.75 \text{ K km s}^{-1}$.

Even if viewed as entirely distinct (because it originates at galactic latitudes well above those typically sampled in galactic plane surveys) the diffuse gas contribution to the total seen looking down on the Milky Way from outside would be $0.47/(0.47+0.75) = 38\%$, a surprisingly high fraction given the supposed absence of molecular gas and CO emission at higher galactic latitudes. The alternative, that the diffuse gas is already incorporated in galactic plane surveys, makes the majority of the gas ($0.47/0.75$) in the galactic plane diffuse. This is an even more radical proposition, but is consistent with finding that the preponderance of the molecular gas seen toward the heavily-extincted line of sight toward B0355+508 at $b = -1.6^\circ$ is actually diffuse.

In fact, the extent of the diffuse and/or high-latitude contribution to the local CO emission remains to be determined by wide-field CO surveys whose detection limit is substantially better than 1 K km s^{-1} and perhaps no worse than even 0.25 K km s^{-1} . Assessing the contribution of diffuse gas at lower latitudes awaits a wider examination of the character of the gas seen in the galactic disk, but the contribution of diffuse molecular gas in the inner galactic disk is apparent in recent HERSCHEL/PRISMAS observations of sub-mm absorption spectra toward star-forming regions (Gerin et al., 2010; Sonnentrucker et al., 2010).

10. Summary and conclusions

We compared maps of CO emission with reddening maps on a typical field of view of about $30' \times 30'$ at an angular resolution of $1'$ toward 11 diffuse lines of sight for which we already had sub-arcsec molecular and/or atomic absorption profiles. This allowed us to draw three kinds of conclusions.

10.1. Conclusions about the position-position-velocity structure of the emission

- Although most of the CO emission structure was amorphous or merely blob-like when mapped, the emission around B0528+138 was found to be highly regular and quasi-periodic while that around B2200+420 (aka BL Lac) was seen to be filamentary and tangled.
- Toward B0355+508 and B0528+134, CO mapping suggests that pairs of absorption lines separated by 6-8 km s^{-1} are physically related, not merely accidental superpositions.

Table 3. Components with weak CO emission toward the continuum target^a

| Target | V km s ⁻¹ | $\tau(1-0)$ | T _R [*] K | dN(CO)/dV 10 ¹⁵ cm ⁻² (km s ⁻¹) ⁻¹ | T _{exc} (1-0) K | p(H ₂) 10 ³ cm ⁻³ K | n(H ₂) ^b cm ⁻³ | $\int \tau(\text{HCO}^+) dv / \text{total}$ |
|--------|-------------------------|-------------|----------------------------------|--|-----------------------------|--|---|---|
| B0212 | -10.3 | 0.49 | 0.40 | 0.65 | 3.4-3.6 | 1.9-2.5 | 75-100 | 0.122 |
| | -0.05 | 0.95 | < 0.14 ^c | 1.11 | <3.1-3.2 | <0.9-1.1 | <35-45 | 0.102 |
| B0224 | -10.6 | 0.43 | < 0.10 | 0.48 | <3.0-3.1 | <0.8-1.0 | <30-40 | 0.161 |
| B0355 | -13.9 | 0.45 | 0.31 | 0.52 | 3.8-4.0 | 3.0-3.5 | 120-140 | 0.224 |
| | -4.0 | 0.86 | 0.37 | 1.10 | 3.6-3.8 | 2.1-2.5 | 85-100 | 0.204 |
| B0528 | 2.8 | < 0.11 | < 0.16 | | | | | 0.080 |
| B1730 | 5.1 | 1.15 | 0.24 | 1.42 | 3.5-3.7 | 1.8-2.2 | 70-90 | 1.000 |
| B1928 | -3 | < 0.11 | < 0.11 | | | | | 1.000 |

^a Using CO parameters originally derived by Liszt & Lucas (1998) and $\tau(\text{HCO}^+)$ from Lucas & Liszt (1996)

^b At T_K = 25 K

^c Upper limits in this column are 2 σ

- CO mapping shows that partition of an absorption profile into kinematic components, no matter how seemingly obvious, may actually be arbitrary and capricious: the decomposition may have no apparent validity in emission at positions only slightly removed from the continuum background.

10.2. Conclusions linking the absorption to the emission kinematics:

- The same clouds were seen in absorption and emission, and in atomic and molecular phases, although not necessarily in the same location. We failed to find CO emission corresponding to just one out of 20 molecular absorption features, in one relatively small spatial field, i.e. 20' × 20' vs. 30' × 30' or more. Conversely, while mapping away from the continuum background we saw only 2 CO emission features lacking molecular absorption counterparts.
- CO emission was sometimes found in the field at velocities corresponding to features seen only in H I absorption toward the continuum. We saw no molecular features outside the span of the H I absorption.

10.3. Conclusions regarding the CO luminosity of diffuse gas.

- We found relatively bright CO emission at modest reddening in the fields we mapped, with peak brightnesses of 4-5 K at E_{B-V} ≲ 0.15 mag and up to 10-12 K at E_{B-V} ≈ 0.3 mag (i.e. A_V ≈ 1 mag). This was true even for features that were seen only in absorption toward the continuum source in the field center.
- The CO emission lines represent small column densities N(CO) ≤ 10¹⁶ cm⁻², less than 10% of the amount of free gas phase carbon expected along a line of sight with E_{B-V} = 0.15 mag or A_V = 0.5 mag. The dominant form of gas phase carbon is still C⁺.
- When CO emission was detected at levels of 1.5 K km s⁻¹ and higher, it was generally over-luminous in the sense of having a small ratio N(H₂)/W_{CO}, i.e. a value of the CO-H₂ conversion factor below 2 × 10²⁰ H₂ (K km s⁻¹)⁻¹. W_{CO}/N(H₂) ratios as small as N(H₂)/W_{CO} ≲ 5 × 10¹⁹ cm⁻² H₂ (km s⁻¹)⁻¹ are mandated by the observed reddening in cases where the line of sight was relatively free of extraneous material.
- On the whole, the W_{CO}/N(H₂) ratio in diffuse gas is the same as in dense fully molecular clouds despite the presence of strong variations between individual diffuse gas parcels or

sightlines. The global W_{CO}/N(H₂) ratio in diffuse gas is the result of averaging over limited regions where CO emission is readily detectable and overly bright (in the sense of having W_{CO}/N(H₂) much higher than the mean), and with other regions having a significant molecular component (as seen in absorption) but where CO emission is comparatively weak or simply undetectable.

- Small W_{CO}/N(H₂) ratios and sharp variations in the W_{CO}/E_{B-V} ratio are not artifacts of the disparity in resolution between the 1' CO emission beam and the 6' resolution of the reddening maps, because high CO brightnesses and small W_{CO}/E_{B-V} ratios persist when the resolution of the CO maps is degraded to that of the reddening maps.
- Sharp variations in the CO emission brightness on arcminute scales do not necessarily represent unresolved structure in the reddening maps or in the column density of H or H₂. Detectable CO emission generally arises in the regime where W_{CO} ∝ N(CO), and variations in the line brightness represent primarily the CO chemistry with its extreme sensitivity to E_{B-V} and N(H₂). Secondly the line brightness is influenced by CO rotational excitation since some features are not seen in emission toward continuum sources where there is CO absorption with appreciable optical depth.
- Only peripherally does the CO brightness represent the underlying mass or H₂ column density distribution of diffuse molecular gas.

Acknowledgements. The National Radio Astronomy Observatory is operated by Associated Universities, Inc. under a cooperative agreement with the US National Science Foundation. The Kitt Peak 12-m millimetre wave telescope is operated by the Arizona Radio Observatory (ARO), Steward Observatory, University of Arizona. IRAM is operated by CNRS (France), the MPG (Germany) and the IGN (Spain). This work has been partially funded by the grant ANR-09-BLAN-0231-01 from the French *Agence Nationale de la Recherche* as part of the SCHISM project (<http://schism.ens.fr/>). We thank Edith Falgarone for comments that inspired Sections 8.4 and 8.5 of this work.

References

- Abdo, A. A., Ackermann, M., Ajello, M., Baldini, L., Ballet, J., Barbiellini, G., Bastieri, D., Baughman, B. M., Bechtol, K., Bellazzini, R., Berenji, B., Bloom, E. D., Bonamente, E., Borgland, A. W., Bregeon, J., Brez, A., Brigida, M., Bruel, P., Burnett, T. H., Buson, S., Caliandro, G. A., Cameron, R. A., Caraveo, P. A., Casandjian, J. M., Cecchi, C., Celik, Ö., Chekhtman, A., Cheung, C. C., Chiang, J., Ciprini, S., Claus, R., Cohen-Tanugi, J., Cominsky, L. R., Conrad, J., Dermer, C. D., de Palma, F., Digel, S. W., Silva, E. d. C. e., Drell, P. S., Dubois, R., Dumora, D., Farnier, C., Favuzzi, C., Fegan, S. J., Focke, W. B., Fortin, P., Frailis, M., Fukazawa, Y., Funk, S., Fusco, P., Gargano, F., Gehrels, N., Germani, S., Giavitto, G., Giebels, B., Giglietto, N., Giordano, F., Glanzman, T., Godfrey, G., Grenier, I. A., Grondin, M.-H., Grove, J. E., Guillemot, L., Guiriec, S., Harding, A. K.,

- Hayashida, M., Horan, D., Hughes, R. E., Jackson, M. S., Jóhannesson, G., Johnson, A. S., Johnson, W. N., Kamae, T., Katagiri, H., Kataoka, J., Kawai, N., Kerr, M., Knödlseeder, J., Kuss, M., Lande, J., Latronico, L., Lemoine-Goumard, M., Longo, F., Loparco, F., Lott, B., Lovellette, M. N., Lubrano, P., Makeev, A., Mazziotta, M. N., McEnery, J. E., Meurer, C., Michelson, P. F., Mitthumsiri, W., Mizuno, T., Monte, C., Monzani, M. E., Morselli, A., Moskalenko, I. V., Murgia, S., Nolan, P. L., Norris, J. P., Nuss, E., Ohsugi, T., Okumura, A., Omodei, N., Orlando, E., Ormes, J. F., Paneque, D., Pelassa, V., Pepe, M., Pesce-Rollins, M., Piron, F., Porter, T. A., Rainò, S., Rando, R., Razzano, M., Reimer, A., Reimer, O., Reposeur, T., Rodriguez, A. Y., Ryde, F., Sadrozinski, H. F.-W., Sanchez, D., Sander, A., Saz Parkinson, P. M., Sgrò, C., Siskind, E. J., Smith, P. D., Spandre, G., Spinelli, P., Starck, J.-L., Strickman, M. S., Strong, A. W., Suson, D. J., Takahashi, H., Tanaka, T., Thayer, J. B., Thayer, J. G., Thompson, D. J., Tibaldo, L., Torres, D. F., Tosti, G., Tramacere, A., Uchiyama, Y., Usher, T. L., Vasileiou, V., Vilchez, N., Vitale, V., Waite, A. P., Wang, P., Winer, B. L., Wood, K. S., Ylinen, T., Ziegler, M., & Fermi/LAT Collaboration. 2010, *ApJ*, 710, 133
- Bania, T. M., Marscher, A. P., & Barvainis, R. 1991, *Astron. J.*, 101, 2147
- Berné, O., Marcelino, N., & Cernicharo, J. 2010, *Nature*, 466, 947
- Burgh, E. B., France, K., & McCandliss, S. R. 2007, *ApJ*, 658, 446
- Dame, T. M., Hartmann, D., & Thaddeus, P. 2001, *ApJ*, 547, 792
- Dame, T. M. & Thaddeus, P. 1994, *ApJ*, 436, L173
- Dickey, J. M., Kulkarni, S. R., Heiles, C. E., & Van Gorkom, J. H. 1983, *Astrophys. J., Suppl. Ser.*, 53, 591
- Gerin, M., de Luca, M., Goicoechea, J. R., Herbst, E., Falgarone, E., Godard, B., Bell, T. A., Coutens, A., Kaźmierczak, M., Sonnentrucker, P., Black, J. H., Neufeld, D. A., Phillips, T. G., Pearson, J., Rimmer, P. B., Hassel, G., Lis, D. C., Vastel, C., Boulanger, F., Cernicharo, J., Dartois, E., Encrenaz, P., Giesen, T., Goldsmith, P. F., Gupta, H., Gry, C., Hennebelle, P., Hily-Blant, P., Joblin, C., Kolos, R., Krelowski, J., Martín-Pintado, J., Monje, R., Mookerjee, B., Perault, M., Persson, C., Plume, R., Salez, M., Schmidt, M., Stutzki, J., Teyssier, D., Yu, S., Contursi, A., Menten, K., Geballe, T. R., Schlemmer, S., Morris, P., Hatch, W. A., Imram, M., Ward, J. S., Caux, E., Güsten, R., Klein, T., Roelfsema, P., Dieleman, P., Schieder, R., Honingh, N., & Zmuidzinas, J. 2010, *A&A*, 521, L16
- Gir, B.-Y., Blitz, L., & Magnani, L. 1994, *ApJ*, 434, 162
- Goldreich, P. & Kwan, J. 1974, *ApJ*, 189, 441
- Hartmann, D. & Burton, W. B. 1997, *Atlas of galactic neutral hydrogen* (Cambridge; New York: Cambridge University Press)
- Heithausen, A. 2004, *ApJ*, 606, L13
- Hily-Blant, P. & Falgarone, E. 2009, *A&A*, 500, L29
- Hogerheijde, M. R., De Geus, E. J., & Spaans, F. 1995, *ApJ*, 441, L93
- Jenkins, E. B. & Tripp, T. M. 2011, *ApJ*, 734, 65
- Lequeux, J., Allen, R. J., & Guilleaume, S. 1993, *A&A*, 280, L23
- Liszt, H. & Lucas, R. 2001, *A&A*, 370, 576
- Liszt, H., Lucas, R., & Pety, J. 2006, *A&A*, 448, 253
- Liszt, H. S. 1994, *ApJ*, 429, 638
- 2007, *A&A*, 476, 291
- Liszt, H. S. & Lucas, R. 1996, *A&A*, 314, 917
- 1998, *A&A*, 339, 561
- 2000, *A&A*, 355, 333
- Liszt, H. S., Pety, J., & Lucas, R. 2010, *A&A*, 518, A45+
- Liszt, H. S., Pety, J., & Tachihara, K. 2009, *A&A*, 499, 503
- Liszt, H. S. & Wilson, R. W. 1993, *ApJ*, 403, 663
- Lucas, R. & Liszt, H. S. 1993, *A&A*, 276, L33
- 1996, *A&A*, 307, 237
- 2000, *A&A*, 358, 1069
- Maddalena, R. J. & Morris, M. 1987, *ApJ*, 323, 179
- Magnani, L., Blitz, L., & Mundy, L. 1985, *ApJ*, 295, 402
- Marscher, A. P., Bania, T. M., & Wang, Z. 1991, *ApJ*, 371, L77
- Pety, J. & Falgarone, E. 2003, *A&A*, 412, 417
- Pety, J., Lucas, R., & Liszt, H. S. 2008, *A&A*, 489, 217
- Planck Collaboration, Ade, P. A. R., Aghanim, N., Arnaud, M., Ashdown, M., Aumont, J., Baccigalupi, C., Balbi, A., Banday, A. J., Barreiro, R. B., & et al. 2011, *A&A*, 536, A19
- Rachford, B. L., Snow, T. P., Destree, J. D., Ross, T. L., Ferlet, R., Friedman, S. D., Gry, C., Jenkins, E. B., Morton, D. C., Savage, B. D., Shull, J. M., Sonnentrucker, P., Tumlinson, J., Vidal-Madjar, A., Welty, D. E., & York, D. G. 2009, *Astrophys. J., Suppl. Ser.*, 180, 125
- Sakamoto, S. & Sunada, K. 2003, *ApJ*, 594, 340
- Savage, B. D., Drake, J. F., Budich, W., & Bohlin, R. C. 1977, *ApJ*, 216, 291
- Schlegel, D. J., Finkbeiner, D. P., & Davis, M. 1998, *ApJ*, 500, 525
- Sheffer, Y., Rogers, M., Federman, S. R., Abel, N. P., Gredel, R., Lambert, D. L., & Shaw, G. 2008, *ApJ*, 687, 1075
- Sheffer, Y., Rogers, M., Federman, S. R., Lambert, D. L., & Gredel, R. 2007, *ApJ*, 667, 1002
- Shetty, R., Glover, S. C., Dullemond, C. P., & Klessen, R. S. 2011, *MNRAS*, 412, 1686
- Smith, A. M., Stecher, T. P., & Krishna Swamy, K. S. 1978, *ApJ*, 220, 138
- Snow, T. P. & McCall, B. J. 2006, *Ann. Rev. Astrophys. Astron.*, 44, 367
- Sonnentrucker, P., Neufeld, D. A., Phillips, T. G., Gerin, M., Lis, D. C., de Luca, M., Goicoechea, J. R., Black, J. H., Bell, T. A., Boulanger, F., Cernicharo, J., Coutens, A., Dartois, E., Kaźmierczak, M., Encrenaz, P., Falgarone, E., Geballe, T. R., Giesen, T., Godard, B., Goldsmith, P. F., Gry, C., Gupta, H., Hennebelle, P., Herbst, E., Hily-Blant, P., Joblin, C., Kolos, R., Krelowski, J., Martín-Pintado, J., Menten, K. M., Monje, R., Mookerjee, B., Pearson, J., Perault, M., Persson, C. M., Plume, R., Salez, M., Schlemmer, S., Schmidt, M., Stutzki, J., Teyssier, D., Vastel, C., Yu, S., Caux, E., Güsten, R., Hatch, W. A., Klein, T., Mehdì, I., Morris, P., & Ward, J. S. 2010, *A&A*, 521, L12
- Sonnentrucker, P., Welty, D. E., Thorburn, J. A., & York, D. G. 2007, *Astrophys. J., Suppl. Ser.*, 168, 58
- Yamamoto, H., Onishi, T., Mizuno, A., & Fukui, Y. 2003, *ApJ*, 592, 217

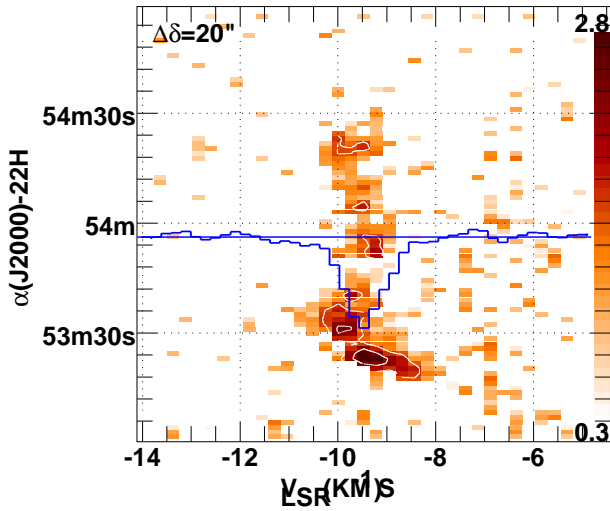


Fig. A.1. A right ascension-velocity diagram of CO emission 20'' North of B2251+158. The CO absorption spectrum toward B2251 is shown with its 0-level at the location of the continuum source; the peak absorption is 22%, see Fig. 7. Contours are shown at levels 1, 2, 3, ... K.

Appendix A: CO line kinematics around 3 additional objects

Shown in Figs. A.1 - A.3 are position-velocity diagrams in right ascension across the positions of B2251+ 158, b0212+735 and B0224+671. As in Figs. 13 and 14 in the main text, the HCO⁺ absorption spectrum toward the continuum background target is superposed in the figures with its baseline positioned where the diagram most nearly crosses the location of the continuum. These diagrams are intended to show how the features that occur in the absorption line profiles are somewhat haphazard samples of the larger scale gas distribution traced in CO emission but toward B0212+735 the diagram also indicates how the CO emission underrepresents the molecular gas distribution.

Appendix B: The galaxy viewed in atomic gas around the background targets

To provide context for the kinematics seen in the present work, Figs. B.1 and B.2 show large-galactic-scale H I latitude-velocity diagrams for each of the sources studied here, using results of the LDSS survey of Hartmann & Burton (1997). The spatial resolution of these data is 35' and the data are on a 30' grid. The diagrams were constructed at the galactic longitude nearest the background target (see Table 1). The latitudes of the sources are marked. Even if it was not apparent from the overlap of the H I and molecular absorption in the figures in the text, these maps make it clear that the molecular gas studied here is part of "normal" galactic structure, mixed into the general ISM.

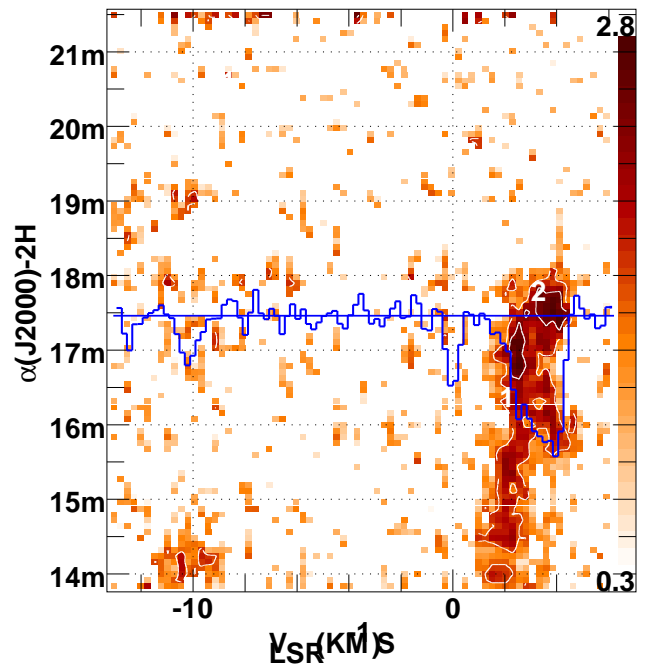


Fig. A.2. A right ascension-velocity diagram of CO emission across the field of B0212+735. The CO absorption spectrum toward B0212 is shown with its 0-level at the location of the continuum source; the strongest absorption line is quite opaque, see Fig. 10. Contours are shown at levels 1, 2, 3, ... K.

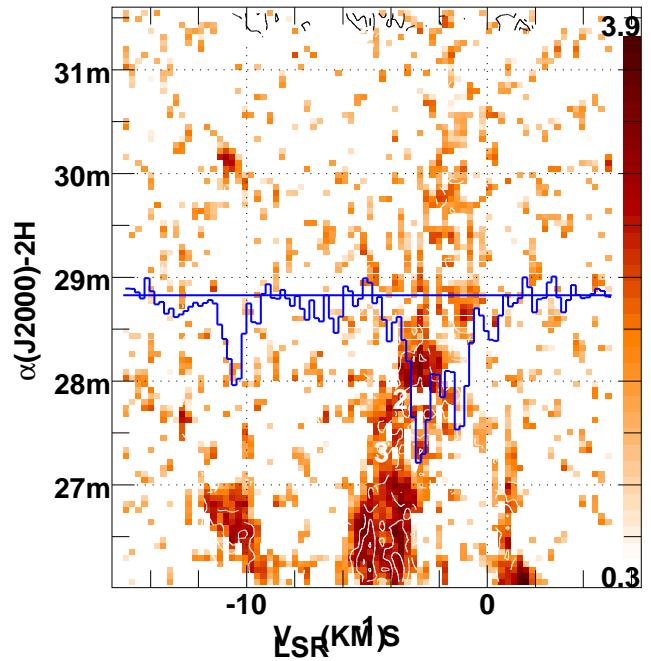


Fig. A.3. A right ascension-velocity diagram of CO emission across the field of B0224+671 at the declination of the continuum source. The CO absorption spectrum toward B0224+671 is shown with its 0-level at the location of the continuum source; the peak optical depth is 1.2, see Fig. 11. Contours are shown at levels 1, 2, 3, ... K.

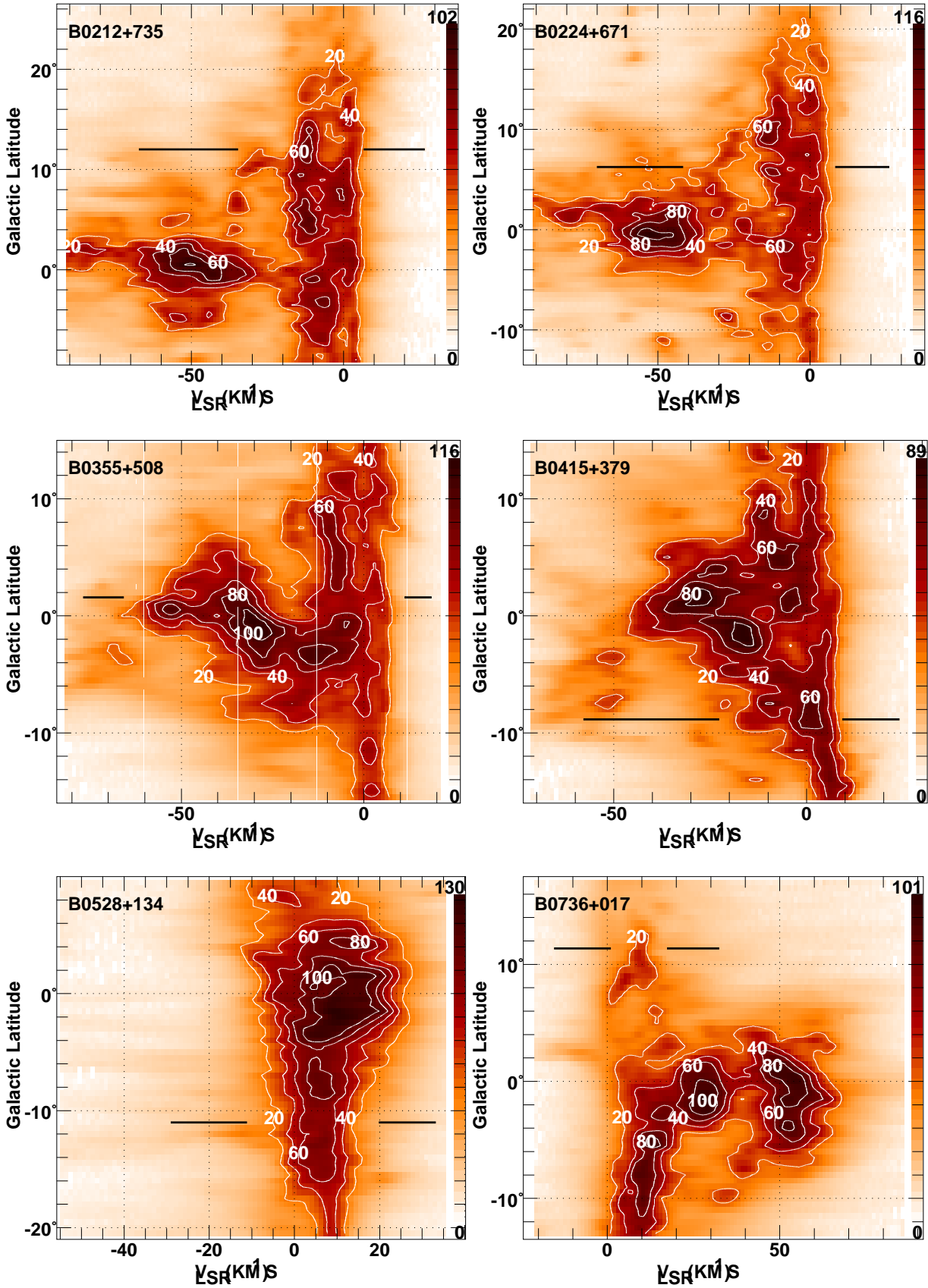


Fig. B.1. Latitude-velocity diagrams of H I brightness around six background targets used for mm-wave molecular absorption studies, using H I data from the LDSS survey (Hartmann & Burton, 1997). The spatial resolution is 35' and the diagrams were constructed at the nearest longitude on the 0.5° grid of the survey datacube. The latitudes of the sources are marked. The line of sight toward B0415+379 (3C111) is not discussed in this work.

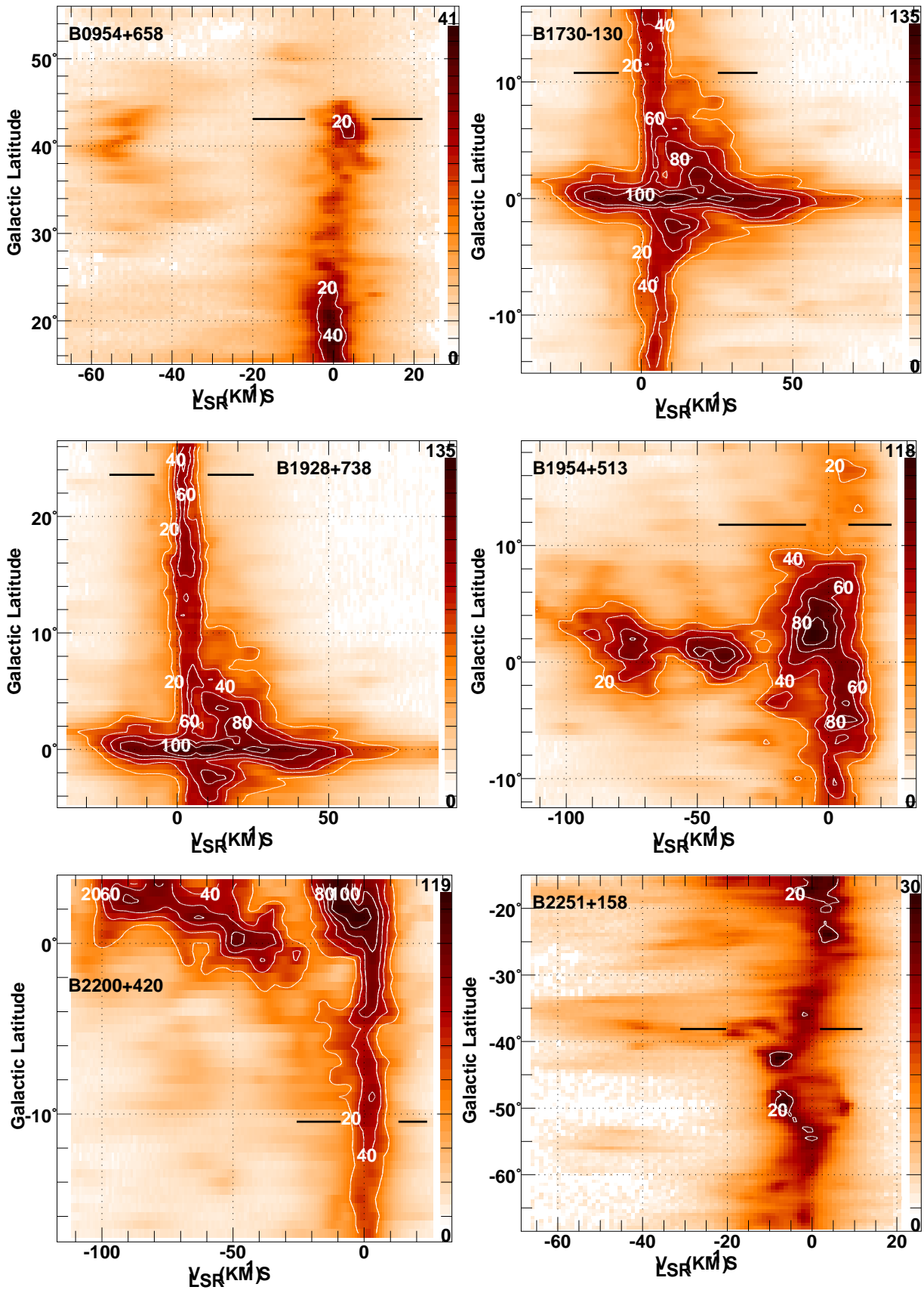


Fig. B.2. Latitude-velocity diagrams of H I brightness around six background targets used for mm-wave molecular absorption studies, using H I data from the LDSS survey (Hartmann & Burton, 1997), as in Fig. B.1